Prepared for *Marine and Petroleum Geology*

Figures: 11

Tables: 2

Words: 9200

Title:

Pore habit of methane hydrate and its evolution in sediment matrix – laboratory visualization with phase-contrast micro-CT

Authors:

Liang Lei[1], Yongkoo Seol[1,*], Jeong-Hoon Choi[1,2], Timothy J Kneafsey[3]

[1] National Energy Technology Laboratory, U.S. Department of Energy, Morgantown, WV 26507

[2] AECOM, Morgantown, WV 26507

[3] Energy Geosciences Division, Lawrence Berkeley National Laboratory, University of California, Berkeley, CA 94720

Email: Yongkoo.Seol@netl.doe.gov

Abstract

Describing the pore habit of methane hydrate in sediment matrices is essential for understanding natural distribution of methane hydrate, methane trace (transport and solidification) in the hydrate stability zone, physical properties of hydrate-bearing sediments, and the associated influence on potential gas production. Pore habit visualization in natural media at pore scale even with laboratory synthesized cores has been challenging due to the similar densities of methane hydrate from pore liquid. In this work, we used phase-contrast assisted micro-CT with potassium iodine-doped brine to visualize four phases: sand particles, pore fluid, methane hydrate and methane gas. This study visualizes the pore habit of methane hydrate at various stages including during hydrate formation in excess-gas systems, its evolution after brine injection to replace pore fluid, and hydrate formation in excess-water systems. Hydrate tends to adopt round and smooth surfaces when in contact with water while exhibits relatively angular interfaces when in contact with methane gas. Hydrate formation in excess-gas systems results in a partial cementing and partial mineral-coating pore habit, while hydrate in excess-water systems develops mainly as pore-filling, and locally cementing or mineral-coating where big gas pockets exist at the initial state. Pore liquid replacement from methane gas to brine triggers a shift of hydrate pore habit towards pore-filling. Methane hydrate evolution over time produces bigger hydrate particles but with less contact area with sand particles. The effects of hydrate pore habit become less important as hydrate particle size exceeds the pore size. Additionally, hydrate formation could trap residual methane gas and brine as inclusions.

45**Keywords**

46Methane hydrate, Pore habit, Phase-contrast micro CT, Contact angle

1. Introduction

Gas hydrate has gained increasing attention due to its great potential to impact climate and to serve as a new energy resource [*Boswell*, 2009; *Boswell and Collett*, 2011; *Collett et al.*, 2010]. Research on hydrate has expanded from laboratory studies to pressure core testing and field tests [*Choi et al.*, 2014; *Dallimore et al.*, 2012; *Lee et al.*, 2013; *Li et al.*, 2018; *Santamarina et al.*, 2015; *Waite and Spangenberg*, 2013; *Yamamoto et al.*, 2014], yet our understanding of physical properties of hydrate bearing sediments is still limited. Hydrate pore habit, that is where hydrate exists within the pore space of a porous medium, fundamentally affects the physical properties of hydrate-bearing sediments (HBS). An understanding of this is critical for gas production, including practical estimations of gas production rate, well stability, sea floor settlement etc., as it determines hydrological and geomechanical properties of the sediments [*Boswell et al.*, 2017; *Li et al.*, 2018; *Shin and Santamarina*, 2017; *Waite et al.*, 2008; *Waite et al.*, 2009]. Quite a few models have been developed based on idealized habit assumptions including: cementing, pore-filling, mineral-coating, and load-bearing to attribute them to the overall properties of the hydrate bearing sediments [*Chand et al.*, 2006; *Dvorkin et al.*, 2000; *Kleinberg et al.*, 2003; *Spangenberg*, 2001]. These models are frequently used to infer hydrate saturations based on field measurements of wave velocities and electrical conductivities as well as to estimate the potential behavior of the reservoir [*Ghosh et al.*, 2010; *Shankar and Riedel*, 2011; *Wang et al.*, 2011; *Weitemeyer et al.*, 2011]. Recent studies use these conceptual assumptions to curve-fit the relation between hydrate saturation and sediment acoustic properties of laboratory synthesized cores [*Yun et al.*, 2007] and field measurements of wave velocities [*Kleinberg and Dai*, 2005; *Winters et al.*,

722011]. Micromodel studies have also provided insights in 2.5 dimension transparent
73systems under reasonable conditions [*Almenningen et al.*, 2017; *Hauge et al.*, 2016;
74*Katsuki et al.*, 2006; *Katsuki et al.*, 2007; *Katsuki et al.*, 2008; *Tohidi et al.*, 2002;
75*Tohidi et al.*, 2001], however these systems do not have realistic mineral surface
76and roughness, or a third dimension. To the best of our knowledge, there is no pore-
77scale study providing direct observations on pore habit of methane hydrate to date.

Micro-Computed Tomography (CT) has been extensively used to study hydrate-bearing sediments [*Choi et al.*, 2011; *Jin et al.*, 2006; *Jin et al.*, 2005; *Lee et al.*, 2013; *Rees et al.*, 2011; *Seol and Kneafsey*, 2009; *Yun et al.*, 2011]. Its non-destructive nature enables the 3D visualization of the inner structure of a specimen while the specimen is kept under hydrate stable pressure and temperature conditions. Over time, reported CT results tend to show increasing resolution from microns [*Jin et al.*, 2008; *Lei and Santamarina*, 2018; *Ta et al.*, 2015] to even sub-microns [*Chaouachi et al.*, 2015; *Sell et al.*, 2016; *Yang et al.*, 2016]. Although spatial resolution is improving, attenuation resolution is a major remaining challenge because methane hydrate has similar X-ray attenuation coefficients to water, which make it difficult to separate water from hydrate. Surrogate hydrate forming gases such as Krypton or Xenon have been used to distinguish the hydrate from the fluid phase [*Chaouachi et al.*, 2015; *Chen and Espinoza*, 2018], or alternately, an enhancing agent such as potassium iodide (KI) has been often added to the water phase without optimization on concentration [*Kerkar et al.*, 2014; *Ta et al.*, 2015]. The salt contained in water can shift the phase boundary of methane hydrate [*Sloan and Koh*, 2008], and ion-exclusion during hydrate formation [*Egeberg and Dickens*, 1999; *Hesse*, 2003] as well as freshening effect during hydrate dissociation [*Milkov et al.*, 2004] also make the hydrate behavior different from that in deionized water; but natural hydrate formation mostly occurs in brine environments. However, 3D structure of methane hydrate within pore space and its response to various disturbances have yet to be investigated with direct high resolution visualization approach.

We have used high resolution micro CT scanning to visualize the 3-D occurrence, habit, and behavior of methane hydrate in sediment matrices. Our tests

aim to mimic natural conditions, where a large amount of gas invades a hydrate stability zone and accumulates underneath a seal layer resulting in a local excess-gas system. Here, water saturation may vary and only 'immobile' water is left in the local environment, resulting in pendular water being enclosed by connected gas accumulations. Secondly, as the hydrate formation consumes the gas, surrounding brine will flow in to replace pore fluid, which would incur pore habit evolution. We model this by brine injection into the excess-gas-formed hydrate. Lastly, we also examine hydrate formation in excess-water (non-connected gas phase) systems by examining the condition where a small amount of gas bubbles are trapped in the sediment during their upward migration and gas hydrate forms in such excess-water system. We will present the pore habit of methane hydrate and its evolution over the sequential transitions of hydrate-contacting fluid filling in pore space. The wettability of hydrate crystals to the quartz surface and morphology of single hydrate crystals, as well as the hydrate growth patterns will be discussed with respect to hydrate's interaction with sediment components. Based on our observations, pore habit of methane hydrate in natural conditions will be projected.

2. Experiment

2.1 Experiment configuration

Specimen preparation. Ottawa sand 40/70 (210-380 μm in diameter, mean grain size 250 μm), and deionized water were used to prepare the initial specimen. F110 sand (70-150 μm in diameter, mean grain size 120 μm) was used for one layer in ExG-KI-1 (See Table 2 for further details), packed on top of the 40/70 Ottawa sand. Before placing the sand in the sleeve, the sand was mixed with water to achieve desired water contents and then packed into the rubber sleeve. The total

core volume was 1.71 ml (d = 6.35 mm, h = 54 mm), and the pore volume was ~0.6±0.07 ml with a porosity of ~0.35±0.04 (segmented from CT images). Following hydrate formation, 5 wt% of KI (SIGMA-ALDRICH, purity > 99%) solution was flushed through the specimen to replace the pore fluid. Paper filters were placed on both ends of the specimen to prevent sand particle migration and potential clogging inside connecting lines.

Seven experiments were performed and scanned using an XRadia Micro-CT 400. Figure 1 shows the experiment configuration adopted in this study. We used a beryllium X-ray transparent core holder that provides a confining stress to the specimen by applying fluid pressure to an elastomer sleeve containing the specimen. The core holder was placed on a Peltier plate underlain by an aluminum plate that serves both as the mounting base and heat dissipator. The whole configuration inside the cabinet of micro-CT scanner was always connected to pressure and power sources via flexible lines and cables to ensure unstrained rotation of the core holder during the scans.

Control of temperature, pressure and effective stress. Temperature was controlled using a Peltier plate that extracted heat from the specimen via the beryllium core holder and transferred to the aluminum plate for dissipation. The region of the coreholder that was X-ray CT scanned was covered with a plexiglas jacket filled with dry air for thermal insulation. The air-filled jacket was designed to minimize noise in CT images that can appear when random pattern foam-type insulation materials are used. The beryllium core holder is a good thermal conductor, yet there was still a temperature gradient along the specimen (~0.7 °C/cm), i.e., a temperature difference of ~4 °C between the top and bottom of the specimen, due to the single Peltier plate on the bottom of the core holder. We used

syringe pumps to control pore pressure (flow injection and receiving, ISCO 500 HP) and confining pressure (ISCO 100 DX). The radial effective stress (confining pressure minus pore pressure) was kept constant to maintain a steady soil skeleton. The pore pressure was measured by a pressure transducer (Setra 204E, 0-20.7 MPa (0-3000 psi), ±0.11% FS) on the injection side. The back pressure in the receiving ISCO pump was equilibrated with the the pore pressure transducer each time before injections. Temperature measurement was made by a thermocouple (OMEGA TJC36, K type, diameter 254 μm (0.01 inch)) inserted into the specimen to a depth of ~6 mm from the top.

CT scans. The X-ray micro CT scanner used in this study was an Xradia/Zeiss 400. Three modes of CT scans were used in this study (Table 1): 1) quick overview scan; 2) middle resolution scan; and 3) high resolution scan. The middle resolution scans were performed to check the status of hydrate formation/fluid migraiton processes while the high resolution scan was only taken when the system was relatively stable. Figures 4-7 present post-processed CT images with colored phases for better guided visualization, while raw images in Figures 8, 9 and 11 are presented to focus on image quality variations and intrepretations of featured artifacts. As with general CT images, the CT images display the average condition of the specimen during the scan period, not an image at a single point in time. A particular voxel in the pore space could be occupied by phase one (e.g. methane gas) earlier and phase two (e.g. hydrate) later during the scan. This is particularly important for the high resolution extended scans. Interface movements caused by processes such as hydrate formation and bubble collapse can occur during the scan. Well-defined boundaries indicate stable interfaces between constituents of the specimen during a scan period, e.g., distinct sand surface indicates a stable

sediment skeleton, whereas blurred interfaces capture transient processes (e.g. blue lines encircled areas in Figures 8). Detailed CT scan configuration, image contrast enhancement via phase-contrast CT and optimization of KI solution concentration, and related image processing techniques are covered in *Lei et al.* [2018].

2.2 Experiment purpose and procedure

Experiment purpose & simulated natural conditions. Current experimental simulations aim to mimic natural conditions where hydrate reservoir develops. We present seven independent experiments that contain three hydrate formation/evolution paths. 1) A large quantity of gas invades the hydrate stability zone and accumulates underneath a seal layer to create a local excess-gas system with only 'immobile' water left. The first stage of our experiments is to simulate hydrate formation under the excess-gas condition. 2) As the hydrate formation consumes the gas, surrounding water would flow in. The second stage of the test is to reproduce such conditon with brine injection flooding pore space. 3) Hydrate formation in excess-water systems is simulated lastly by creating a condition where a certain amount of gas bubbles are trapped in the sediment under hydrate stability condition; these gas bubbles may be locally interconnected, but are eventaully enclosed by water. Table 2 lists pressure, temperature, saturation of each phase at each stage, and duration of each experiment step. Figure 2 provides the pressure and temperature trajectories used in all the experiments.

Excess-gas hydrate formation. Excess-gas hydrate formation was emulated in five experiments (labeled ExG) where gas was free to percolate. In the earliest experiment (ExG-KI-1) we lowered the temperature first before taking a reference

CT scan, then introduced the gas flow into the specimen during pressurization. The gas flow caused water movement that disturbed the reference point for comparison in 3D CT images, which results in difficulties understanding the differences between the original reference state and later stages caused by hydrate formation or gas flow associated processes. To enable the comparison between sequences of images, in the other four experiments we increased the pore pressure and confining pressure to the targeted value first before conducting the reference scan, and then changed the temperature. When hydrate formation was triggered by temperature decrease after the reference scan, the shift of mass distribution in the specimen was only due to hydrate formation. All five experiments except ExG-KI-2 in Table 1 were left undisturbed for a minimum of 48 hours so that the systems could approach equilibrium on hydrate formation before CT scanning.

Hydrate evolution during and after KI solution injection. Three experiments (labeled ExG-KI) were performed to determine the influence of KI solution injection, and monitor the evolution of hydrate pore habit after the brine injection. In these tests, about 2 pore volumes of 5 wt% of KI solution were injected into the specimens from the bottom under hydrate-stable pressure and temperature conditions. To accompish this, the pressure in the receiving pump was decreased to drive the flow. The pressure difference between the flow in and out was less than 200 kPa. Fresh KI solution was injected to eliminate methane gas dissolving into the solution, in order to avoid potential clogging in the injection lines. We were able to inject KI solution through the specimen at the pre-step pressure and temperature conditon in ExG-KI-1 and ExG-KI-3 (See Table 2 for specific pressure and temperature values), but had to increase the specimen temperature close to methane hydrate phase boundary in ExG-KI-2 to remove clogging.

Excess-water hydrate formation. In experiment ExW-1 hydrate was reformed by decreasing the temperature in the same specimen used for experiment ExG-KI-3 (after hydrate dissociation by temperature increase in a closed system). The water was already methane saturated and the hydrate formation was under excess-water condition. Here we define this excess-water condition as the isolated gas bubbles or larger gas pockets occupying several connected pores entrapped in water-saturated sediments (Figure 8a). The gas supply was limited to these isolated gas pockets, and the water in the specimen was entirely inter-connected. The water contained dissolved KI in ExW-1. Experiment ExW-2 started with a specimen initially saturated with high pressure methane gas at low temperature, then flooded with deionized water to form hydrate with the residual gas trapped in pores. The injected deionized water did not contain dissolved methane.

Hydrate dissociation. Thermal stimulation or depressurization were used to trigger hydrate dissociation at the end of all the experiments. When thermal stimulation was used (ExG-KI-3 and ExG-2), the temperature was gradually increased in a closed system, that is, the valves on both ends of the specimen were closed. The confining pressure increased at the same rate as pore pressure, maintaining constant effective stress. Hydrate dissociation in the rest of the experiments was attained through depressurization. Constant effective stress was maintained during all dissociation experiments except ExG-1, where the confining pressure was kept at 13.79 MPa with zero pore pressure. CT scans were conducted after dissociation.

3. Results

3.1 Pressure-temperature signatures

Figure 3a shows the typical pressure and temperature response observed when hydrate formed in our experiments. Temperature spikes were less than 1 °C when hydrate started to grow after nucleation, and there was a corresponding pressure drop indicating gas consumption due to hydrate formation. The pressure drop stopped as hydrate formation ceases and temperature reaches its asymptotic value. Note that even after the pressure and temperature appeared to be stable, hydrate morphology evolved continuously during our experiments. The CT scan performed the first day after the temperature spike usually contains noisy images showing blurred interfaces indicating interface movement and phase evolution.

The pressure-temperature trajectory during hydrate dissociation by thermal stimulation is displayed in Figure 3b. The hydrate phase boundary shifted to a lower temperature or higher pressure as the ion (KI) concentration in water increased. Hydrate started to dissociate at the shifted phase boundary when hydrate was in contact with the pore fluid at the concentrated ionic concentrations (~8% KI), but the pressure-temperature trajectory moved towards the methane hydrate phase boundary of deionized water as the released water freshened the pore fluid and diluted the ion concentration. The hydrate dissociation was complete when the KI solution was diluted to ~2%, indicated by the cease of pore pressure increase despite of the imposed temperature increase by turning off the Peltier plate. The KI concentration was lower than 5% because water was released from the initial hydrate in place. The ion concentration change during the hydrate dissociation was consistent with the decrease in brightness of KI solution in CT images.

3.2 Observations from CT images

Phase identification in CT images. The brightness of different phases in 3D reconstructed images corresponds to the average of their attenuation coefficients weighted based on the effective spectrum of the specific CT scan configuration [*Lei et al.*, 2018]. There are 5 different phases in CT images in this study, and the brightness follows the order from highest: sand > KI solution > deionized water ≈ methane hydrate > methane gas. The brightness of KI solution increases with the KI concentration, which can be an indirect signal of hydrate formation or dissociation that concentrates or dilutes the pore fluid. Apart from the brightness, the use of phase contrast CT yields bright-dark pair patterns induced by density differences at the interfaces between neighboring phases, in particular sand-water (KI solution), sand-gas, as well as sand-hydrate. Note that deionized water cannot be separated definitively from methane hydrate in CT images based on the brightness contrasts or the bright-dark pair patterns without the additional enhancement from the added KI. The contact between methane hydrate and gas is distinguishable, however not a smooth interface (Figure 9), which is quite different from the smooth interface between liquid and gas determined by Laplace equation (Figure 8a). We use the interface roughness to verify the existence of a hydrate shell enclosing the gas phase in Figure 9.

Note that the bright-dark pair pattern between sand and hydrate in our CT images is not caused by the water film. Reported thickness of water film on ice surfaces is no more than 100 nm at -1 °C [*Furukawa et al.*, 1987; *Smit and Bakker*, 2017], which is far smaller than the resolution of the CT scanner, while the diffraction induced pair pattern is ~ 3 μm on average between the bright-dark pair edges.

Excess-gas hydrate formation experiments (ExG). At the low water saturation used, the gas phase was connected throughout the specimen and hydrate formation was limited by the availability of water. Figures 4a and 4b show the image attenuation shifts (image of interest minus reference image) on X-ray projections at selected times of 5 minutes (a) and 81 hours (b) after the temperature spike. Red areas indicate added mass compared to the initial case before the temperature spike with uniform water distribution. There was fast water movement within 24 hours after the temperature spike, shown as concentrated mass gain areas in the upper center of the core in Figure 4a. The mass migration slowed down noticeably after the first 24 hour period, and approached equilibrium (Figure 4b) between 24 hours and 81 hours after the temperature spike. This observation is consistent with previous P-wave measurements with larger specimens [*Choi et al.*, 2014], where both wave velocity and amplitude increased rapidly during the first 24 hours after the temperature spike before stabilized over ~60 hours after the temperature spike. In our tests, hydrate formation was the only driving force for water movement, which has been confirmed with another complementary experiment (not documented here) where an identical core showed no obvious mass migration patterns without hydrate formation.

The 3D reconstructed images (Figure 4c) focusing on the top portion of the 2D projection in Figure 4b show two clearly distinguishable regions, either filled with hydrate (lower half) or with methane gas (upper half). The 3D scan with higher resolution (Figure 4d) reveals even clearer hydrate separation from other phases. Note that the highlighted area is a small portion of the specimen, and because mass can exchange throughout the specimen, mass conservation within the highlighted area does not apply.

Figure 4e displays the mass migration with time. The local hydrate saturation S_h at the end of formation is ~95% in slice B and 0% in slice A. In Slice A there were signs of hydrate formation during 7h-20h. Later, mass moved away and the hydrate volume gradually diminished. In Slice B, water moved out initially after the temperature spike (7h-20h) but flowed back during the continuous hydrate formation period as hydrate formation drew water from the surrounding area and hydrate saturation increased (30h-43h and 68h-81h). The evolution sequence on slice B suggests that the pore space was mainly filled with hydrate. During the entire course of hydrate formation, the pressure remained constant while the temperature oscillated over a range of ~1.5 °C. Note that the CT images alone cannot differentiate deionized water from hydrate; therefore it is not guaranteed that all the blue area in Figure 4e is filled with hydrate. Yet the sequence of images in Figure 4e reveals the history of hydrate growth over extended period. Interpretation of CT images is based on not only the pixel intensity but also morphology and morphology evolution: hydrate is with rough edges; while water is with smooth interfaces.

Figure 5 shows relatively stable hydrate formed at least 54 hours after the temperature spike. Note that all the hydrate particles are attached to an adjacent sand surface. Some of the hydrate may appear suspended in 2D slices (Figures 5a and b), but in 3D view, they are attached to neighboring sand particles. Individual hydrate particles tend to have rounded shapes where hydrate saturation S_h = 5% and 13%. Hydrate starts to connect adjacent sand particles as hydrate saturation increases to 13%. This hydrate provides new contacts other than the original sand-to-sand contact points to the sand skeleton, important for geomechanical and geophysical properties. As hydrate saturation increases to 25%, hydrate particles

spread on sand surfaces and form finger-like spreading patterns of hydrate that display rough surfaces and limited thickness as shown in Figures 5c, (more similar observations can be found in Figure 7c and 7h with zoomed 3D view), and hydrate often connects adjacent sand particles. The thickness of hydrate in the direction perpendicular to the sand surface is usually less than ~40 μm across the specimen (Figure 5c). Meanwhile, we observed no thin layer or film-like hydrate coating on sand surfaces. Irregularly shaped residual gas pockets fill up the rest of pore space when hydrate saturation S_h increases to 95% (Figures 5d and 4e-slice B).

During and after brine injection. KI brine was injected at pressure and temperature conditions either deep inside the methane hydrate stability field in experiments ExG-KI-1 and ExG-KI-3 (12.41 MPa, 10 °C and 10.69 MPa, 5 °C, respectively) or close to the phase boundary in ExG-KI-2 (6.89 MPa, 9 °C). Most of the hydrate formed under unsaturated condition was preserved at its original location during the brine injection when the injection pressure and temperature condition occurred deep within methane hydrate stability field (Figure 6a, c and d). In contrast, we suspect that hydrate could be detached from the sand surface, flow along with the brine and congregate in bigger pores if pressure and temperature conditions are close to phase boundary (Figure 6b, ExG-KI-2). Some of the hydrate particles observed in a large pore space (Figure 6b) appear to be attached to adjacent hydrate particles rather than on the sand surface, implying that they detached from the original formation location and were transported to the current location. Also note that the hydrate distribution in Figure 6b is concentrated in the big pores, which could serve as the main flow channels, while hydrate particles in the other three tests are relatively well distributed. Local hydrate saturation in 6d is higher than in 6c because the small pores in 6d preserved more water initially

before hydrate formation under the excess-gas condition.

Hydrate morphology evolved quickly after the KI solution injection. Hydrate in brine-saturated pores tends to have a smoother surface than that in direct contact with methane gas. The contact area between hydrate and sand particle greatly reduced as hydrate got bigger and rounder (3D view in Figures 7h and 7i). Some of the hydrate that was originally 'cementing' adjacent sand particles got redistributed towards a pore-filling hydrate, which could contribute to the decrease in overall stiffness or wave velocities of the specimen [*Choi et al.*, 2014 & 2018]. As hydrate morphology changed with KI solution injection, it is clear that the contact angle between hydrate and sand particle mostly became larger than 90 degrees in brine environment (see the 3D view in Figure 7i), which implies that the sand surface has more affinity to water than hydrate. Contact angle at certain spots in Figure 7i looks smaller than 90 degrees because: 1) there are areas with trapped gas (see Figure 7f); 2) the transition of hydrate pore habit is still ongoing.

There was gas left behind after KI solution flushes (Figures 6 and 7d). The amount of trapped gas increased with hydrate saturation as hydrate sealed more fluid flow paths. Additional hydrate formed from the KI solution and residual gas, resulting in a hydrate volume increase (compare Figures 7d-f).

Hydrate formation in excess-water (brine) condition. Gas supply was limited in excess-water hydrate formation (ExW-1 and ExW-2) (Figure 8). The specimen after dissociation driven by temperature increase in ExG-KI-3 was used as the starting point of Experiment ExW-1. Hydrate formed during cooling under the excess-water condition occurred initially at the brine-gas interface. This turned into a layer of hydrate along the brine-gas interface. As hydrate reformation consumed gas, the gas pressure became lower than the surrounding water pressure. When the

pressure difference supported by the hydrate shells exceeded the strength of the shell, the shell cracked, and brine invaded into the gas pocket resulting in hydrate forming in spikes as shown in the yellow circled area (Figure 8b). Hydrate continued to grow into gas pockets with the additional supply of water and most of the gas pockets disappeared within 6 days. Small bubbles transformed into hydrate particles (green circle enclosed area in Figures 8b and 8d) in the first 2 days, which later became larger as they experienced Ostwald ripening. As water was consumed during hydrate formation, KI concentrated in the residual solution. Note the initial hydrate in Figure 8 was very heterogeneous in texture with gas and brine inclusions, and it ripened to form larger and rounder hydrate particles (green circle enclosed area).

Experiment ExW-2 used deionized water rather than brine in the hydrate formation (Figure 9). Hydrate shell formation and cracking occurred in ExW-2. Massive hydrate spikes formed in the circled area where there was a big methane bubble initially, and these spikes transformed into a complex network. Although it is clear the methane gas and deionized water is separated by hydrate shells, difficulties remain in the determination of hydrate saturation in the specimen because of the density resolution of the CT scans: the thickness of the hydrate shell is unknown, and there could be hydrate particles in pores that appears to be saturated with water.

An earlier effort [*Choi et al.*, 2014] used thermal cycles after brine flooding to dissociate existing hydrate formed in excess-gas conditions and re-form hydrate in excess-water conditions. The resulting hydrate pore habit, although not verified with pore-scale observation, should resemble those observed in this experiment, i.e., mainly pore-filling, which is also consistent with their P-wave velocity

measurements.

4. Analyses and discussion

The observed hydrate distributions and its evolution pattern in pore space described above help improve current understanding on hydrate nucleation, hydrate formation and associated mass migration, and resulting hydrate pore habit. This section provides outcomes of detailed analysis on such issues, as well as further discussion on anticipated characteristics of naturally occurring hydrate, and implications on hydrate-bearing systems based on the experimental observations.

4.1 Hydrate nucleation

Hydrate nucleation is critical as it is a precursor for later hydrate pore habit and distribution pattern. Three potential mechanisms at various water contents include nucleation at the water-gas interface, on small water droplets clinging to the sand surface, and from dissolved methane in pore spaces filled with water.

Hydrate nucleation preferentially occurs on water-gas interfaces and more often on sand-water-gas contact lines, and frequently forms a shell covering the interface (See examples in [*Servio and Englezos*, 2003; *Subramanian*, 2000]). To induce hydrate formation, pressurization of a pre-cooled system could be effective for prompt nucleation with mechanical stimulations associated with the pressurization process, compared to the pre-pressurized system with post-cooling. The nucleation in the pre-cooled system with post pressurization can be further expedited by micro water droplets formed on the sand surface with cooling. When the initial water saturation is low (< ~10%) so that gas can freely percolate, cooling before pressurization allows water condensation on sand surfaces first before

hydrate nucleation. Cooling from T = 22 °C to 5 °C (data from [*Hardy*, 1998]) could cause water vapor pressure drop from 2.65 kPa (density ρ = 19.4 grams/m^3) to 0.9 kPa (ρ = 6.8 grams/m^3). The reduced moisture in vapor phase corresponds to 1.2×10^{-5} volume of dew in 1 unit volume of pore space, or a ~1 µm diameter droplet in a pore space with 50 µm in diameter.

The third nucleation mechanism for hydrate nucleation from dissolved methane molecules in methane saturated water [*Spangenberg et al.*, 2005] has not been observed in our experiments because we cannot detect hydrate formation in water phase with our micro CT observations.

4.2 Hydrate growth and mass migration

Hydrate formation is a dynamic process, as shown in Figure 4, governed by various thermodynamic and hydrochemical mechanisms such as mass migration of hydrate forming constituents, heat transfer and pressure equilibrium, and salting out with high salinity in brine. When these processes occur in non-uniform poroelastic skeleton, the resulting hydrate distribution patterns and pore habit can significantly vary locally with dominant pore filling fluid changes. Hydrate formation displays distinctive features under excess-gas conditions, excess-water conditions, and during the transition between these conditions, and hydrate growth patterns under these sets of conditions reveal corresponding mass migration mechanisms.

Hydrate growth over sand particle surfaces. Our experiments clearly show hydrate growing over sand particle surfaces in both excess-gas (e.g., Figures 7a and 7c) and excess-water cases. The sand surfaces in contact with methane gas in Figure 8a are mostly covered by a layer of hydrate in Figure 8c (area in red circle). The hydrate growth covering the mineral surface has also been observed in glass

micromodels (Figure 2B in *Tohidi et al.* [2001]). The initial water saturation (isolated cyan spots in Figure 7g) is not able to support locally concentrated hydrate in Figure 7h and mechanisms for water migration are required. Hydrate generally formed throughout porous medium is mostly inter-connected in 3D space, which implies that the water supply path can be associated with the hydrate network, via either hydrate-methane gas interface or hydrate-sand interface. If the water migration is via the hydrate-methane gas interface, it would be more likely that the transported water would thicken the hydrate layer rather than to move towards the hydrate formation front (Figure 10a), thus it would be more plausible to expect water migrate between the hydrate and sand. Furthermore, hydrate often forms shells at the water-gas interface under excess-water conditions, and the water migration via hydrate-methane gas interfaces (e.g. area in the red circle in Figure 8b) would not be feasible, therefore the water supply to the formation front over sand particles is very likely to be via the water film between sand and hydrate. The water migration driven by capillarity via water film between hydrate and sand surfaces facilitates hydrate formation near the original water menisci initially (Figure 10a) and the additional hydrate formation extends the water supply path so that hydrate formation advances further. This mechanism helps to extract water from other parts of the specimen to fill ~20% of the pore volume in the scanned area in Figure 7, and the transport distance is farther than 2.3 mm (~10 particles).

Hydrate growth into gas pockets. Hydrate growth into gas pockets has been widely observed under excess-water condition. Hydrate spikes observed in this scenario could resemble the ice spikes [*Libbrecht and Lui*, 2004] and “soda straw stalactites” [*Curl*, 1972]. The center of the tube serves as a water conduit to further facilitate hydrate growth into the gas space (Figure 11c). Hydrate growth in the

spike form happens at multiple spots randomly and continues until the gas in the pockets becomes depleted or it hits the other side. Hydrate spike formation with brine (Figures 8b and 11b) seems much shorter in length than those with deionized water (Figures 9 and 11a). The ion-exclusion process creates a local spot with high salinity around the spike tip, which prevents further tube-like hydrate growth (Figure 11d). Note that this mechanism of hydrate formation is different from the formation of hair-like or needle-like hydrate crystals reported in *Servio and Englezos* [2003] and *Lei and Santamarina* [2018].

Extended hydrate evolution via diffusion. The hydrate morphology evolves after its initial formation, mainly via diffusion driven by concentration gradients of water vapor in methane gas or dissolved methane in brine/water. This concentration gradient is associated with the difference in hydrate crystal sizes (Figures 10b and 10c). Water vapor migration in excess-gas condition is via diffusion in methane gas therefore is fast for both short (sub-pore to pore) range and long range (pore to cm scale) transport when compared with diffusion of dissolved methane in water phase. The water vapor diffusion occurs between standalone hydrate particles, as well as between hydrate in different parts of the specimen. For example slices A and B in Figure 4 show evidence of transport distance longer than 1.2 mm (~5 particles). In contrast, in excess-water systems, dissolved methane transport via diffusion in water could be four orders of magnitude slower [*Cussler*, 2009] therefore it's range of impact is relatively short (estimated to be mainly within the same pore) at the limited laboratory time scale. Diffusion of dissolved methane occurs when cementing and mineral-coating hydrate formed under the excess-gas cases evolves towards pore-filling hydrate after brine injection, and between hydrate particles with different sizes, which facilitates Ostwald ripening.

4.3 Morphology of single hydrate particles

Micro-CT cannot distinguish single hydrate crystals from polycrystalline masses, and even though some of the hydrate particles appear to originate from more than one hydrate nuclei, “particles” here refers to these hydrate masses.

Hydrate particle surface: round or angular? The majority of particles appears angular under excess-gas conditions (Figure 5), including local gas pockets under excess-water conditions (Figure 8 and 9). By contrast, all the hydrate in contact with brine exhibited round surfaces (e.g., after KI injection into excess-gas systems or excess-water/brine condition). Such hydrate particle morphology may result from two major conditions; (1) brine as a contacting phase and (2) pressure-temperature conditions near the hydrate phase boundary. The stable crystal shape is dependent on the interfacial free energy, which tends to be minimized as a crystal form, whether it is in contact with methane gas with water vapor or water with dissolved methane, in accordance with the Wulff construction [*Herring*, 1951]. In addition, a stable crystal surface can shift from having facets to round when the pressure-temperature condition approaches to hydrate phase boundary, which is commonly known as roughening effect, also observed in hydrate formation in micromodels [*Katsuki et al.*, 2006; *Katsuki et al.*, 2007]. The salt contained in the pore fluid, which gets further concentrated as more hydrate forms, could shift the methane hydrate phase boundary close to the actual pressure-temperature condition of the hydrate in the experiment, and this boundary shift in brine environment could trigger roughening effect. Extensive investigations, however, have yet to be performed to gain insights on dominant mechanisms on evolving hydrate surface morphology.

Contact angle. The contact angle of hydrate on quartz sand surface under excess-water conditions is close to 120° while it ranges from 40° to 100° under excess-gas conditions (estimated from 3D views in CT images). The Young-Dupre equation expresses the contact angle as a function of mutual interfacial tensions (Figure 10d):

$$\gamma_{bs}=\gamma_{as}+\gamma_{ab}\cos\theta_{ab} \quad (1)$$

where γ is the interfacial tension, subscripts *a*, *b* and *s* refer to substrates *a* and *b* and the solid quartz *s*, and θ is the contact angle. There are three cases in our experiments: substituting [h, g], [h, w], and [w, g] for [a, b] in Equation 1, where h, w, and g stand for hydrate, water, and gas respectively. We obtain the following relation with the three equations in these cases:

$$\gamma_{hg}\cos\theta_{hg}=\gamma_{hw}\cos\theta_{hw}+\gamma_{wg}\cos\theta_{wg} \quad (2)$$

The contact angle θ_{wg} of water on quartz surface when in contact with methane is ~40° estimated from Figure 8a within its 3D environment. We assume that the interfacial tension between hydrate and methane gas or water equals to that between ice and gas or water, i.e., γ_{hg} = 109 mJ/m^2 [*Mason*, 1971] and γ_{hw} = 33 mJ/m^2 [*Anderson*, 2003; *Hillig*, 1998]. Also, the interfacial tension between water and high pressure methane could be extrapolated from [*Massoudi and King*, 1974] γ_{wg} = 56965 mJ/m^2 (P = 11 MPa, and T = 25 °C). Then equation (2) is satisfied if θ_{hg} = 72° and θ_{hw} = 120°, which are consistent with our observations. Note that the contact angle is not the same along the sand-hydrate-water or sand-hydrate-gas contact line since the surface free energy of the hydrate lattice varies as a function of orientation. Therefore, it is an average contact angle. This contact angle analysis indicates that quartz surface favors water rather than methane hydrate in excess-water case, but slightly prefers hydrate to methane gas in excess-gas systems.

576

577**4.4 Hydrate pore habit**

578 We have discussed hydrate habits in pore space with varied water
579saturations and proposed hypotheses on mass migration mechanisms supporting
580the hydrate habits observed in this study. Insights into hydrate pore habit is critical
581when the dynamic processes including heat flow, fluid migration, seismic wave
582transmission, and mechanical integrity under evolving stress condition are major
583concerns for predicting behavior of hydrate-bearing reservoir upon stimulations.
584This section will review existing concepts of pore habit and discuss refined concepts
585based on new observations from this study. For the discussion, we use four types of
586hydrate pore habit: cementing, mineral coating, pore-filling, and load bearing,
587proposed by [*Waite et al.*, 2009].

5881) Cementing hydrate is defined as hydrate present at sediment contact points,
589 which significantly increases the contact area between adjacent sand particles. It
590 is widely hypothesized that hydrate formed under excess-gas conditions will
591 have a cementing habit resembling the shape of pendular water menisci. Our
592 observation shows cementing hydrate is irregular in shape. The contact angle
593 between the hydrate and sand surface is different than that between water and
594 sand surface indicating that the hydrate is less wetting (but still wetting) to the
595 silica sand, and it also varies with location. Furthermore, hydrate formation is
596 likely to draw some of the water away from the pendular rings to sustain hydrate
597 growth along sand surfaces, and it often accompanies with mineral-coating
598 hydrate.

5992) Mineral coating habit develops as hydrate grows on sand surfaces under excess-
600 gas conditions. This hydrate growth advances in limited preferred directions

(similar to a fingering effect, see Figure 7h for examples) rather than uniform surface coating. A uniform thin layer of hydrate coating on sediment surfaces often referred in the literature conflicts with our observation.

3) Pore-filling hydrate is often misleadingly depicted in schematics in the literature as particles floating in the pore space. Our observations are that pore-filling hydrate grows attached to the sand surface outward to fill the pore space. In addition, pore-filling hydrate has a contact angle of ~120° under excess-water conditions and its growth is away from the sand surface.

4) The concept of load bearing hydrate is from the mechanical point of view. We highlight that hydrate can bear the load [*Yun et al.*, 2007] and subsea samples have been collected of hydrate veins which has to bear load, although hydrate is not necessarily bearing the load. Hydrate in this study does not bear load even though hydrate fills pore space as high as 74% as there is no discernable sediment skeleton deformation during hydrate formation or dissociation under constant effective stress of 1.38 MPa. The main reason is that the load has been taken by the sediment skeleton and hydrate formation/dissociation does not change the original stress status.

Cementing hydrate is dominant when the initial water saturation is low, but mineral-coating gains more importance as water saturation increases. All the other hydrate formation processes including isolated hydrate particles on sand surface, hydrate shell in gas pockets, and hydrate spike formation tend to occur primarily in pore-filling hydrate. Multiple hydrate pore habits can coexist, especially as hydrate saturation increases. Idealized grain-coating or pore-filling pore habits are often used in cylindrical tube models, Kozeny type models, and numerical simulations [*Kang et al.*, 2016] to calculate the effective permeability of hydrate-bearing

sediments, and these results could be improved by considering a more realistic hydrate morphology within pore spaces. Besides, previously hypothesized but not observed prior to this study [*Choi et al.*, 2014], is that cementing hydrate can become pore-filling if the conditions are changed from excess-gas to excess-water. This has implications in laboratory research on methane hydrate, and also on understanding the seismic and mechanical properties of natural hydrate-bearing sediments.

4.5 Particle size

All hydrate particles should have similar particle size or similar surface curvature when in equilibrium. Pore size, initial phase saturations (excess-gas or excess-water), and proximity to additional mass supply affect hydrate particle size. Water vapor pressure under excess-gas conditions and methane concentration under excess-water conditions in equilibrium with hydrate particle are proportional to hydrate surface curvature (alternatively inversely proportional to hydrate particle size), and a difference in hydrate particle size could result in Ostwald ripening. Hydrate formation is preferential in small pores under excess-gas conditions, developing hydrate particles in similar sizes in early stage before evolving into larger particles. With Ostwald ripening, the average hydrate particle size grows with time while numbers of particles reduces (e.g., the evolution sequence in Figure 8, note the area in green circles); similar results has been observed with THF hydrate [*Mahabadi et al.*, 2016b]. The size can be mostly larger than 30 microns several days after the initial formation and smaller particles diminish eventually with the pressure and temperature conditions used in this study. Due to varied affinities to neighboring phases, hydrate particles under excess-gas conditions tends to show

larger aspect ratio (longer dimension vs. shorter dimension), compared to circular particles under excess-water condition.

If the pore size in the sediment is smaller than the average hydrate particle size, for example, 30 microns in this study, the hydrate particles almost completely fill some of the pores but leave the rest empty (See small pores in Figure 6d). In this case, a patch type hydrate distribution forms [*Dai et al.*, 2012] and distinction of pore habit would not be significant anymore; and patchy hydrate distribution exhibits unique mechanical and hydrological behaviors [*Dai et al.*, 2012; *Mahabadi et al.*, 2019; *Mahabadi et al.*, 2016a]. On the other hand, in coarse sediments with larger pores, hydrate particles can adopt abovementioned pore habits depending on the formation condition. Published experiments on sands have been using a large range of particle sizes, from 100 μm to 3000 μm [*Chen and Espinoza*, 2018; *Choi et al.*, 2014; *Ta et al.*, 2015], and pore size varies in an even wider range in natural layered subsea sands and sub-arctic sands. Special attention should be paid to the particle and pore size when interpreting the influence of pore habit on the associated physical properties.

4.6 Trapped fluid

Hydrate can trap some fluid such as methane gas and brine with elevated salt concentration (Figure 8), especially when hydrate saturations are high. These trapped fluids do not contribute to hydraulic flow, and the measured hydraulic conductivities are the same as if these inclusions were hydrate. The existence of gas can greatly reduce the P-wave velocity in hydrate free sediments due to the sharp reduction in bulk modulus of the overall sediment, while this reduction trend can be dampened when the gas inclusions are covered by thick hydrate shells. The

hydrate saturation estimation based on measured acoustic properties could overestimate the hydrate saturation. Similarly, if the increase of chlorinity due to ion-exclusion during hydrate formation is used to determine hydrate saturation [*Torres et al.*, 2011], the result may not fully reflect the reality since there could be a chlorinity difference between the trapped fluid and connected fluid, especially at high hydrate saturation locations with increasing chances of having trapped fluid.

4.7 Implications to natural hydrate

Laboratory tests to mimic natural hydrate presence and habit are inevitably constrained by limited reaction time, simplified sediment textures, and microscopic scale of the observation range, and any attempts to directly extrapolate laboratory observations to natural phenomena should respect these limitations. Acknowledging the limitations, we have tried to conjecture pore-behavior characteristics of natural methane hydrate emplaced in sandy sediments. Our experimental settings for hydrate formation consisted of excess-gas conditions, followed by brine injection, and excess-water conditions with gas either released from preexisting hydrate or injected. These conditions were designed to mimic natural sand reservoirs with gas-rich layers under saturated formations. Volumetric gas contents in the gas-rich layers can vary widely depending on mechanisms and rates of gas supply, origin of gas, and eventually diminish as gas turns into hydrate and dissolves into migrating water. We expect natural hydrate under stable conditions (sufficient time after initial formation) forming isolated particles, or cementing or mineral-coating hydrate under excess-gas condition initially. Hydrate particles can grow large (>30 μm in diameter) depending on pore sizes or merge together to form more stable hydrate masses. As water migrates into the formation or gas get consumed by hydrate

formation creating excess-water condition, cementing or mineral coating hydrate can detach from sand surfaces, particularly near the hydrate stability condition, and/or migrate with water and aggregate in larger pores and evolve towards pore-filling hydrate. Eventually after hydrate formation is completed and the pore space fills with water, hydrate in the pore space would be largely pore-filling, even load bearing if external stress changes the mechanical assembly of particles. In a water-saturated porous medium, pore-filling hydrate is more likely to be encountered, because the sand surface shows more affinity to water (contact angle $\theta_{hw} \approx 120°$ if silica sand) than to hydrate. Important however is that the pore-filling hydrate has less contact area with sand particles. If the hydrate is initially formed in excess-gas environment, some of the cementing hydrate could grow into bigger hydrate particles and preserve the initial cementing portion (Compare yellow circled area in Figures 7d and 7c). Therefore, pore habit and the presence and contents of inclusions of natural methane hydrate could be used to infer its formation environment and history. In addition, understanding the behavior of hydrate under these conditions and its dissociation and reforming to respond to changes in the environment help to better predict the mechanical, geophysical, and hydrological properties of hydrate-bearing porous media.

5. Conclusion

This study visualizes the 3D pore habit of methane hydrate and its evolution in porous sediments using micro-CT. Hydrate formation and fluid injection through sand packed specimens under hydrate stable pressure and temperature over 13 days clearly shows that hydrate formation is a very dynamic process. Intense mass migration occurs during hydrate formation. Flowing brine into these specimens

impacts evolution of hydrate habit and its resulting form in brine-saturated environments. The evolution of pore habit reflects equilibration processes to find optimal condition for stable hydrate in response to changes in saturation of phases with varied affinities to each other, the hydrate stability boundary with varying salinity, local gradients in molecular activities including molecular diffusion, and global advective flows of water and gas. These observations captured under varied conditions modeling natural processes using high resolution CT scans provides valuable insights into natural hydrate pore behavior and responses to stimulations. A few key observations can be summarized as follows:

Hydrate nucleation in this study mainly occurs on water-gas interfaces. Dew droplets could be potential nucleation sites in experiments with low initial water saturations.

Hydrate growth is always accompanied by mass migration of hydrate forming constituents. We identify three hydrate growth/evolution mechanisms: hydrate growth over sand particle surfaces, hydrate growth via water/brine invasion into gas pockets featuring hydrate shell breakage and hydrate tubes, and extended hydrate morphology evolution via diffusion of water vapor in excess-gas environments and dissolved methane in excess-water environments.

The hydrate surface tends be round and smooth under excess-water conditions, and relatively angular in excess-gas cases. Contact angle between hydrate and quartz sand under excess-gas conditions ranges from 40° to 100°, and increases to ~120° under excess-water conditions. Hydrate particle size increases with time due to Ostwald ripening and sizes of hydrate particles are similar at given time.

Excess-gas systems host cementing and mineral-coating hydrate and this

hydrate occupies small pores and pore throats first. By contrast, excess-water systems develop mainly pore-filling hydrate preferentially in large pores. Brine injection into excess-gas systems shifts the hydrate pore-habit from cementing and mineral-coating to pore-filling. Pore habit is less important when the hydrate particle size gets larger than the size of pores as the hydrate particles almost completely fill some of the pores but leave the rest empty.

Natural gas hydrate is anticipated to be larger than laboratory formed hydrate particles due to longer exposure to Ostwald ripening, and longer equilibration times, with similar particle sizes in round shape, and mostly pore-filling under brine saturated condition.

Acknowledgement

Liang Lei is supported under an Oak Ridge Institute for Science and Education (ORISE) fellowship granted by NETL. The authors thank Karl Jarvis for the help in experiments and Xuerui Gai for discussions.

Reference

Almenningen, S., J. Flatlandsmo, A. R. Kovscek, G. Ersland, and M. A. Fernø (2017), Determination of pore-scale hydrate phase equilibria in sediments using lab-on-a-chip technology, *Lab on a Chip*, *17*(23), 4070-4076.

Anderson, G. K. (2003), Enthalpy of dissociation and hydration number of carbon dioxide hydrate from the Clapeyron equation, *The Journal of Chemical Thermodynamics*, *35*(7), 1171-1183, doi:http://dx.doi.org/10.1016/S0021-9614(03)00093-4.

Boswell, R. (2009), Is Gas Hydrate Energy Within Reach?, *Science*, *325*(5943), 957-958, doi:10.1126/science.1175074.

Boswell, R., and T. S. Collett (2011), Current perspectives on gas hydrate resources, *Energy & environmental science*, *4*(4), 1206-1215.

Boswell, R., T. S. Collett, E. Myshakin, T. Ajayi, and Y. Seol (2017), The increasingly complex challenge of gas hydrate reservoir simulation, paper presented at 9th International Conference on Gas Hydrates.

Chand, S., T. A. Minshull, J. A. Priest, A. I. Best, C. R. Clayton, and W. F. Waite (2006), An effective medium inversion algorithm for gas hydrate quantification and its application to laboratory and borehole measurements of gas hydrate-bearing sediments, *Geophysical Journal International*, *166*(2), 543-552.

Chaouachi, M., A. Falenty, K. Sell, F. Enzmann, M. Kersten, D. Haberthür, and W. F. Kuhs (2015), Microstructural evolution of gas hydrates in sedimentary matrices observed with synchrotron X-ray computed tomographic microscopy, *Geochemistry, Geophysics, Geosystems*, *16*(6), 1711-1722, doi:10.1002/2015GC005811.

Chen, X., and D. N. Espinoza (2018), Ostwald ripening changes the pore habit and spatial variability of clathrate hydrate, *Fuel*, *214*, 614-622, doi:https://doi.org/10.1016/j.fuel.2017.11.065.

Choi, J.-H., S. Dai, J.-H. Cha, and Y. Seol (2014), Laboratory formation of noncementing hydrates in sandy sediments, *Geochemistry, Geophysics, Geosystems*, *15*(4), 1648-1656, doi:doi:10.1002/2014GC005287.

Choi, J.-H., Y. Seol, R. Boswell, and R. Juanes (2011), X-ray computed-tomography imaging of gas migration in water-saturated sediments: From capillary invasion to conduit opening, *Geophys. Res. Lett.*, *38*(17), L17310, doi:10.1029/2011GL048513.

Collett, T. S., A. Johnson, C. C. Knapp, and R. Boswell (2010), *Natural Gas Hydrates: Energy Resource Potential and Associated Geologic Hazards, AAPG Memoir 89*, AAPG.

Curl, R. L. (1972), Minimum diameter stalactites, *Bulletin of the national speleological society*, *34*(4), 129-136.

Cussler, E. L. (2009), *Diffusion: mass transfer in fluid systems*, Cambridge university press.

Dai, S., J. C. Santamarina, W. F. Waite, and T. J. Kneafsey (2012), Hydrate morphology: Physical properties of sands with patchy hydrate saturation, *Journal of Geophysical Research: Solid Earth*, *117*(B11), B11205, doi:10.1029/2012JB009667.

Dallimore, S., K. Yamamoto, J. Wright, and G. Bellefleur (2012), *Scientific results from the JOGMEC/NRCan/Aurora Mallik 2007-2008 Gas Hydrate Production Research Well Program, Mackenzie Delta, Northwest Territories, Canada*.

Dvorkin, J., M. B. Helgerud, W. F. Waite, S. H. Kirby, and A. Nur (2000), Introduction to physical properties and elasticity models, in *Natural Gas Hydrate*, edited, pp.

815245-260, Springer.
816Egeberg, P. K., and G. R. Dickens (1999), Thermodynamic and pore water halogen
817constraints on gas hydrate distribution at ODP Site 997 (Blake Ridge), *Chemical*
818*Geology*, *153*(1), 53-79, doi:https://doi.org/10.1016/S0009-2541(98)00152-1.
819Furukawa, Y., M. Yamamoto, and T. Kuroda (1987), Ellipsometric study of the
820transition layer on the surface of an ice crystal, *Journal of crystal growth*, *82*(4), 665-
821677.
822Ghosh, R., K. Sain, and M. Ojha (2010), Effective medium modeling of gas hydrate-
823filled fractures using the sonic log in the Krishna-Godavari basin, offshore eastern
824India, *Journal of Geophysical Research: Solid Earth*, *115*(B6), B06101,
825doi:10.1029/2009JB006711.
826Hardy, B. (1998), ITS-90 formulations for vapor pressure, frostpoint temperature,
827dewpoint temperature, and enhancement factors in the range–100 to+ 100 C, paper
828presented at Proceedings of the third international symposium on humidity and
829moisture, Teddington, London, England.
830Hauge, L., J. Gauteplass, M. Høyland, G. Ersland, A. Kovscek, and M. Fernø (2016),
831Pore-level hydrate formation mechanisms using realistic rock structures in high-
832pressure silicon micromodels, *International Journal of Greenhouse Gas Control*, *53*,
833178-186.
834Herring, C. (1951), Some Theorems on the Free Energies of Crystal Surfaces,
835*Physical Review*, *82*(1), 87-93.
836Hesse, R. (2003), Pore water anomalies of submarine gas-hydrate zones as tool to
837assess hydrate abundance and distribution in the subsurface: What have we
838learned in the past decade?, *Earth-Science Reviews*, *61*(1), 149-179,
839doi:https://doi.org/10.1016/S0012-8252(02)00117-4.
840Hillig, W. B. (1998), Measurement of interfacial free energy for ice/water system,
841*Journal of Crystal Growth*, *183*(3), 463-468, doi:http://dx.doi.org/10.1016/S0022-
8420248(97)00411-9.
843Jin, S., J. Nagao, S. Takeya, Y. Jin, J. Hayashi, Y. Kamata, T. Ebinuma, and H. Narita
844(2006), Structural investigation of methane hydrate sediments by microfocus X-ray
845computed tomography technique under high-pressure conditions, *Jpn. J. Appl. Phys.*,
846*45*(7L), L714.
847Jin, S., S. Takeya, J. Hayashi, J. Nagao, Y. Kamata, T. Ebinuma, and H. Narita (2005),
848Structure analyses of methane hydrate sediments by microfocus X-ray CT, paper
849presented at Proceedings of the Fifth International Conference on Gas Hydrates,
850Trondheim, Norway.
851Jin, Y., J. Nagao, J. Hayashi, W. Shimada, T. Ebinuma, and H. Narita (2008),
852Observation of Xe Hydrate Growth at Gas−Ice Interface by Microfocus X-ray
853Computed Tomography, *The Journal of Physical Chemistry C*, *112*(44), 17253-17256,
854doi:10.1021/jp803525m.
855Kang, D. H., T. S. Yun, K. Y. Kim, and J. Jang (2016), Effect of hydrate nucleation
856mechanisms and capillarity on permeability reduction in granular media, *Geophys.*
857*Res. Lett.*, *43*(17), 9018-9025, doi:doi:10.1002/2016GL070511.
858Katsuki, D., R. Ohmura, T. Ebinuma, and H. Narita (2006), Formation, growth and
859ageing of clathrate hydrate crystals in a porous medium, *Philosophical magazine*,
86086(12), 1753-1761.
861Katsuki, D., R. Ohmura, T. Ebinuma, and H. Narita (2007), Methane hydrate crystal
862growth in a porous medium filled with methane-saturated liquid water, *Philosophical*
863*magazine*, *87*(7), 1057-1069.
864Katsuki, D., R. Ohmura, T. Ebinuma, and H. Narita (2008), Visual observation of

865dissociation of methane hydrate crystals in a glass micro model: Production and
866transfer of methane, *Journal of applied physics*, *104*(8), 083514.
867Kerkar, P. B., K. Horvat, K. W. Jones, and D. Mahajan (2014), Imaging methane
868hydrates growth dynamics in porous media using synchrotron X-ray computed
869microtomography, *Geochemistry, Geophysics, Geosystems*, *15*(12), 4759-4768.
870Kleinberg, R. L., and J. Dai (2005), Estimation Of The Mechanical Properties Of
871Natural Gas Hydrate Deposits From Petrophysical Measurements, in *Offshore*
872*Technology Conference*, edited, Offshore Technology Conference, Houston, Texas,
873doi:10.4043/17205-MS.
874Kleinberg, R. L., C. Flaum, D. D. Griffin, P. G. Brewer, G. E. Malby, E. T. Peltzer, and J.
875P. Yesinowski (2003), Deep sea NMR: Methane hydrate growth habit in porous
876media and its relationship to hydraulic permeability, deposit accumulation, and
877submarine slope stability, *Journal of Geophysical Research: Solid Earth*, *108*(B10),
8782508, doi:10.1029/2003JB002389.
879Lee, J. Y., J. W. Jung, M. H. Lee, J. J. Bahk, J. Choi, B. J. Ryu, and P. Schultheiss (2013),
880Pressure core based study of gas hydrates in the Ulleung Basin and implication for
881geomechanical controls on gas hydrate occurrence, *Marine and Petroleum Geology*,
88247(0), 85-98, doi:http://dx.doi.org/10.1016/j.marpetgeo.2013.05.021.
883Lei, L., and J. C. Santamarina (2018), Laboratory Strategies for Hydrate Formation in
884Fine-Grained Sediments, *Journal of Geophysical Research: Solid Earth*, *123*,
8852583+2596, doi:10.1002/2017JB014624.
886Lei, L., Y. Seol, and K. Jarvis (2018), Pore-Scale Visualization of Methane Hydrate-
887Bearing Sediments With Micro-CT, *Geophys. Res. Lett.*, *45*(11), 5417-5426,
888doi:doi:10.1029/2018GL078507.
889Li, J.-f., et al. (2018), The first offshore natural gas hydrate production test in South
890China Sea, *China Geology*, *1*, 5-16, doi:10.31035/cg2018003.
891Libbrecht, K. G., and K. Lui (2004), An investigation of laboratory-grown ice spikes,
892*Journal of Glaciology*, *50*(170), 371-374.
893Mahabadi, N., S. Dai, Y. Seol, and J. Jang (2019), Impact of hydrate saturation on
894water permeability in hydrate-bearing sediments, *Journal of Petroleum Science and*
895*Engineering*, *174*, 696-703, doi:https://doi.org/10.1016/j.petrol.2018.11.084.
896Mahabadi, N., S. Dai, Y. Seol, T. Sup Yun, and J. Jang (2016a), The water retention
897curve and relative permeability for gas production from hydrate-bearing sediments:
898pore-network model simulation, *Geochemistry, Geophysics, Geosystems*, *17*(8),
8993099-3110, doi:doi:10.1002/2016GC006372.
900Mahabadi, N., X. Zheng, and J. Jang (2016b), The effect of hydrate saturation on
901water retention curves in hydrate-bearing sediments, *Geophys. Res. Lett.*, *43*(9),
9024279-4287, doi:doi:10.1002/2016GL068656.
903Mason, B. J. (1971), *The Physics of Clouds*, Oxford, Clarendon Press.
904Massoudi, R., and A. D. King (1974), Effect of pressure on the surface tension of
905water. Adsorption of low molecular weight gases on water at 25.deg, *The Journal of*
906*Physical Chemistry*, *78*(22), 2262-2266, doi:10.1021/j100615a017.
907Milkov, A. V., G. R. Dickens, G. E. Claypool, Y.-J. Lee, W. S. Borowski, M. E. Torres, W.
908Xu, H. Tomaru, A. M. Tréhu, and P. Schultheiss (2004), Co-existence of gas hydrate,
909free gas, and brine within the regional gas hydrate stability zone at Hydrate Ridge
910(Oregon margin): evidence from prolonged degassing of a pressurized core, *Earth*
911*and Planetary Science Letters*, *222*(3), 829-843,
912doi:https://doi.org/10.1016/j.epsl.2004.03.028.
913Rees, E. V. L., J. A. Priest, and C. R. I. Clayton (2011), The structure of methane gas
914hydrate bearing sediments from the Krishna–Godavari Basin as seen from Micro-CT

915scanning, *Marine and Petroleum Geology*, *28*(7), 1283-1293, 916doi:http://dx.doi.org/10.1016/j.marpetgeo.2011.03.015.
917Santamarina, J. C., S. Dai, M. Terzariol, J. Jang, W. F. Waite, W. J. Winters, J. Nagao, J. 918Yoneda, Y. Konno, and T. Fujii (2015), Hydro-bio-geomechanical properties of 919hydrate-bearing sediments from Nankai Trough, *Marine and Petroleum Geology*, *66*, 920434-450.
921Sell, K., E. H. Saenger, A. Falenty, M. Chaouachi, D. Haberthür, F. Enzmann, W. F. 922Kuhs, and M. Kersten (2016), On the path to the digital rock physics of gas hydrate-923bearing sediments – processing of in situ synchrotron-tomography data, *Solid Earth*, 9247(4), 1243-1258, doi:10.5194/se-7-1243-2016.
925Seol, Y., and T. J. Kneafsey (2009), X-ray computed-tomography observations of 926water flow through anisotropic methane hydrate-bearing sand, *Journal of Petroleum* 927*Science and Engineering*, *66*(3–4), 121-132, 928doi:http://dx.doi.org/10.1016/j.petrol.2009.01.008.
929Servio, P., and P. Englezos (2003), Morphology of methane and carbon dioxide 930hydrates formed from water droplets, *AIChE J.*, *49*(1), 269-276.
931Shankar, U., and M. Riedel (2011), Gas hydrate saturation in the Krishna–Godavari 932basin from P-wave velocity and electrical resistivity logs, *Marine and Petroleum* 933*Geology*, *28*(10), 1768-1778.
934Shin, H., and J. C. Santamarina (2017), Sediment–well interaction during 935depressurization, *Acta Geotech.*, *12*(4), 883-895.
936Sloan, E. D., and C. Koh (2008), *Clathrate Hydrates of Natural Gases, Third Edition*, 937CRC Press.
938Smit, W. J., and H. J. Bakker (2017), The surface of ice is like supercooled liquid 939water, *Angewandte Chemie*, *129*(49), 15746-15750.
940Spangenberg, E. (2001), Modeling of the influence of gas hydrate content on the 941electrical properties of porous sediments, *Journal of Geophysical Research: Solid* 942*Earth*, *106*(B4), 6535-6548.
943Spangenberg, E., J. Kulenkampff, R. Naumann, and J. Erzinger (2005), Pore space 944hydrate formation in a glass bead sample from methane dissolved in water, 945*Geophys. Res. Lett.*, *32*(24), n/a-n/a, doi:10.1029/2005GL024107.
946Subramanian, S. (2000), Measurement of Clathrate hydrates Containing Methane 947and Ethane Using Raman Spectroscopy, Colorado School of Mines, Glden, CO.
948Ta, X. H., T. S. Yun, B. Muhunthan, and T. H. Kwon (2015), Observations of pore-949scale growth patterns of carbon dioxide hydrate using X-ray computed 950microtomography, *Geochemistry, Geophysics, Geosystems*, *16*(3), 912-924.
951Tohidi, B., R. Anderson, M. Clennell, J. Yang, A. B. Biderkab, and R. W. Burgass 952(2002), Application of high pressure glass micromodels to gas hydrates studies, 953paper presented at 4th International Conference on Gas Hydrates, Yokohama, 954Japan.
955Tohidi, B., R. Anderson, M. B. Clennell, R. W. Burgass, and A. B. Biderkab (2001), 956Visual observation of gas-hydrate formation and dissociation in synthetic porous 957media by means of glass micromodels, *Geology*, *29*(9), 867-870, doi:10.1130/0091-9587613(2001)029<0867:vooghf>2.0.co;2.
959Torres, M. E., T. S. Collett, K. K. Rose, J. C. Sample, W. F. Agena, and E. J. 960Rosenbaum (2011), Pore fluid geochemistry from the Mount Elbert Gas Hydrate 961Stratigraphic Test Well, Alaska North Slope, *Marine and Petroleum Geology*, *28*(2), 962332-342, doi:https://doi.org/10.1016/j.marpetgeo.2009.10.001.
963Waite, W. F., T. J. Kneafsey, W. J. Winters, and D. H. Mason (2008), Physical property 964changes in hydrate-bearing sediment due to depressurization and subsequent

965repressurization, *Journal of Geophysical Research: Solid Earth*, *113*(B7), n/a-n/a,
966doi:10.1029/2007JB005351.
967Waite, W. F., et al. (2009), Physical properties of hydrate-bearing sediments,
968*Reviews of Geophysics*, *47*(4), RG4003, doi:10.1029/2008RG000279.
969Waite, W. F., and E. Spangenberg (2013), Gas hydrate formation rates from
970dissolved-phase methane in porous laboratory specimens, *Geophys. Res. Lett.*,
971*40*(16), 4310-4315.
972Wang, X., S. Wu, M. Lee, Y. Guo, S. Yang, and J. Liang (2011), Gas hydrate
973saturation from acoustic impedance and resistivity logs in the Shenhu area, South
974China Sea, *Marine and Petroleum Geology*, *28*(9), 1625-1633.
975Weitemeyer, K., S. Constable, and A. Tréhu (2011), A marine electromagnetic
976survey to detect gas hydrate at Hydrate Ridge, Oregon, *Geophysical Journal*
977*International*, *187*(1), 45-62.
978Winters, W., M. Walker, R. Hunter, T. Collett, R. Boswell, K. Rose, W. Waite, M.
979Torres, S. Patil, and A. Dandekar (2011), Physical properties of sediment from the
980Mount Elbert gas hydrate stratigraphic test well, Alaska North Slope, *Marine and*
981*Petroleum Geology*, *28*(2), 361-380.
982Yamamoto, K., Y. Terao, T. Fujii, T. Ikawa, M. Seki, M. Matsuzawa, and T. Kanno
983(2014), Operational overview of the first offshore production test of methane
984hydrates in the Eastern Nankai Trough, paper presented at Offshore Technology
985Conference, Offshore Technology Conference.
986Yang, L., A. Falenty, M. Chaouachi, D. Haberthür, and W. F. Kuhs (2016),
987Synchrotron X-ray computed microtomography study on gas hydrate decomposition
988in a sedimentary matrix, *Geochemistry, Geophysics, Geosystems*, *17*(9), 3717-3732,
989doi:10.1002/2016GC006521.
990Yun, T. S., C. Lee, J.-S. Lee, J. J. Bahk, and J. C. Santamarina (2011), A pressure core
991based characterization of hydrate-bearing sediments in the Ulleung Basin, Sea of
992Japan (East Sea), *Journal of Geophysical Research: Solid Earth*, *116*(B2), B02204,
993doi:10.1029/2010JB007468.
994Yun, T. S., J. C. Santamarina, and C. Ruppel (2007), Mechanical properties of sand,
995silt, and clay containing tetrahydrofuran hydrate, *Journal of Geophysical Research:*
996*Solid Earth*, *112*(B4), doi:doi:10.1029/2006JB004484.
997

998Table 1. Technical parameters of three types of CT scan configurations. Refer to
999specification of Zeiss/Xradia XCT-400 for further details on the detector.

Scan type	Detector	Resolution [µm]	Voxel number	Scan time [hour]
Overview	Macro 70	10	1024^3	6
Middle resolution	4X	4.6	512^3	13
Fine resolution	4X	2.3 (1.15)	1024^3 (2048^3)	64-76

1000

1001

1002Table 2. Test conditions summary.

Test No.[a]	Steps[b]	t [hour]	P[c] [MPa]	T[c] [°C]	Saturation rate [%][d]			Fig. No.	Pre-step operations	Note
					MH	DI/KI[e]	Gas			
ExG-1	Initial	0-68	13.79	24	0	--	--	--	Sample preparation, then P↑	CP[g]=1.38 MPa
	Hydrate	68-217	13.79	4.5	9	--	91	5	T↓	n[h]=0.30
ExG-2	Initial	0-24	13.79	23	0	27	73	4	Sample preparation, then P↑	CP=1.38 MPa
	Hydrate	24-120	13.79	12	34	0	66	4,5	T↓	n=0.35
ExG-KI-1	Initial	0-72	0	25	0	--	--	--	Sample preparation, then T↓	CP=1.03 MPa
	Hydrate	72-146	12.41	10	35	0	65	5	P↑	n=0.36
	KI	146-308	12.41	10	46	53	1	6	KI injection at current P-T	
ExG-KI-2	Initial	0-5	0	25	0	--	--	--	Sample preparation	CP=1.38 MPa
	Hydrate	5-45	6.89	4	34 (MH+DI)		66	--	P↑, then T↓	n=0.34
	KI	45-120	6.89	4	39	58	3	6	KI injection at T≈T_{ph}[f] to unclog flowlines	
ExG-KI-3	Initial	0-24	10.69	24	0	13	87	7	Sample preparation, then P↑	CP=1.38 MPa
	Hydrate	24-126	10.69	5	33	0	67	5,7	T↓	n=0.37
	KI	126-240	10.69	5	59	36	5	6,7	KI injection at current P-T	
ExW-1	Initial	0-24	11.38	14	0	44	56	8a	T↑ in a closed system from ExG-KI-3	CP=1.38 MPa
	KI	24-240	10.34	4	41	58	1	8b-d,11	T↓	n=0.37
ExW-2	Initial	0-24	11.03	23	0	--	--	--	Sample preparation, P↑ & T↓	CP=1.38 MPa
	Hydrate	24-48	11.03	4.5	92 (MH+DI)		8	9,11	DI flush	n=0.33

1003

1004[a]ExG=Excess-gas condition; ExW=Excess-water condition; KI=KI solution injection.
1005[b]Initial=Condition before hydrate formation; Hydrate=Hydrate exists, maybe together with deionized water;
1006KI=Hydrate coexists with KI solution.
1007[c]Average value, pressure varies when the system is isolated by closed valves during scan and temperature oscillates
1008in each scan.

[d]Segmented from CT images.
[e]DI=Deionized water (text underlined), KI=KI solution.
[f]T_{ph}=Temperature on phase boundary of methane hydrate with current pressure.
[g]CP= lateral effective stress, which equals the difference between confining fluid and pore fluid.
[h]n=porosity, which does not change during hydrate formation/dissociation.

1014Figure 1. Experiment setup showing pressure, temperature and effective stress
1015control, and CT scan configuration.

1016

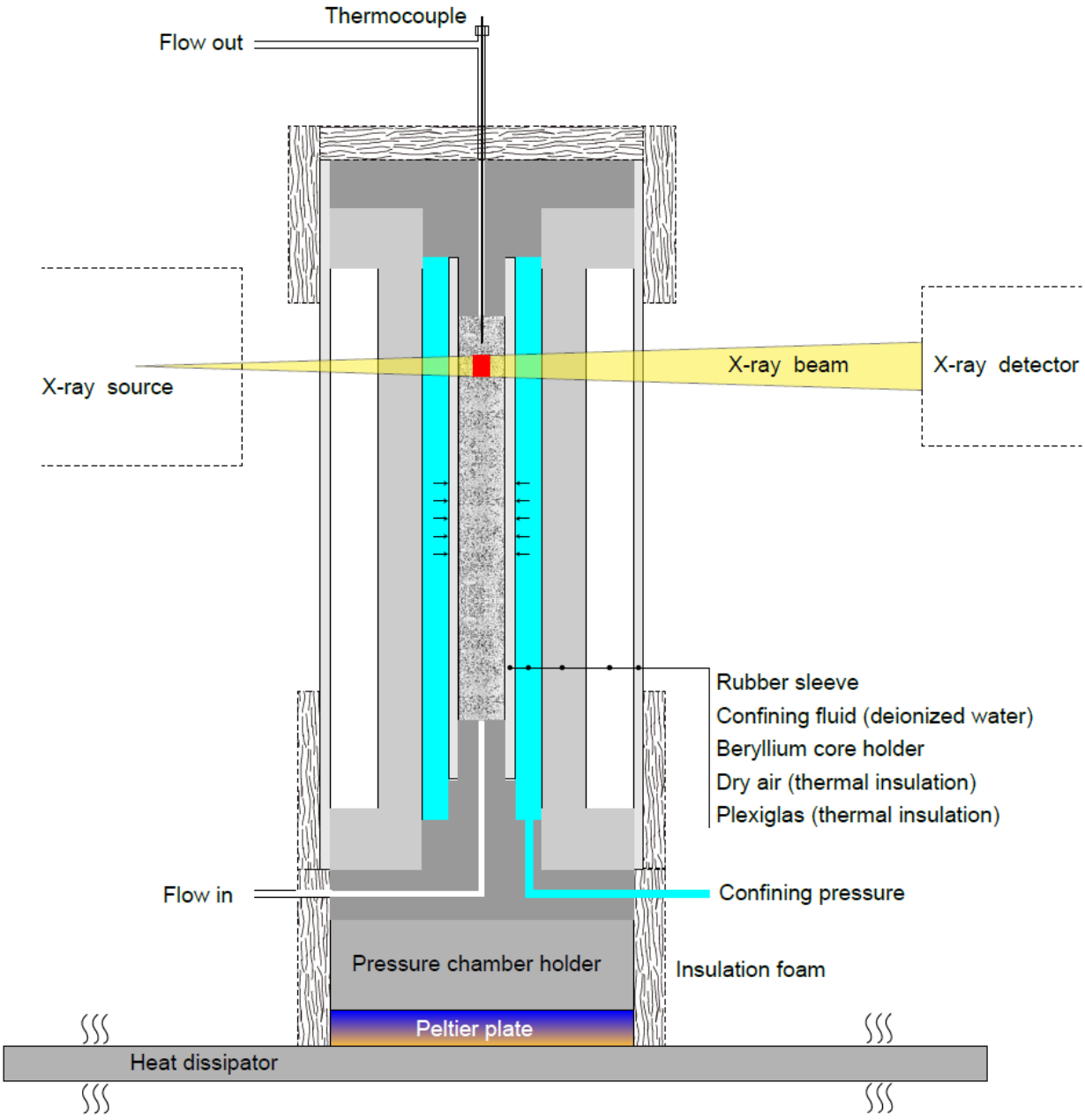

1017

1018

1019Figure 2. Pressure-temperature trajectories during the tests (refer to the numbers in 1020Table 2 for actual pressure and temperature values). Green and blue lines show two 1021paths: a) path: decrease the temperature, conduct the reference scan, and increase 1022pressure to form hydrate, b) path: increase pressure, conduct reference scan, and 1023then decrease temperature to form hydrate. The second row shows the pressure-1024temperature path during brine injection. The third row shows the pressure-1025temperature response of the specimen during hydrate formation triggered by 1026temperature decrease in a closed system.

Pressure-temperature and phase boundary	Pressure and temperature versus time
ExG: a) path Tests included: ExG-KI-1; b) path tests included: ExG-KI-3, ExG-KI-2, ExG-1, ExG-2.	
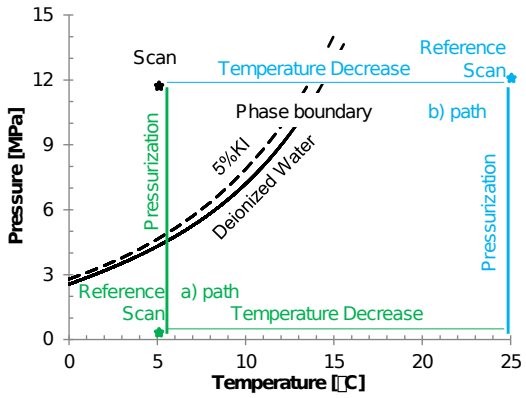	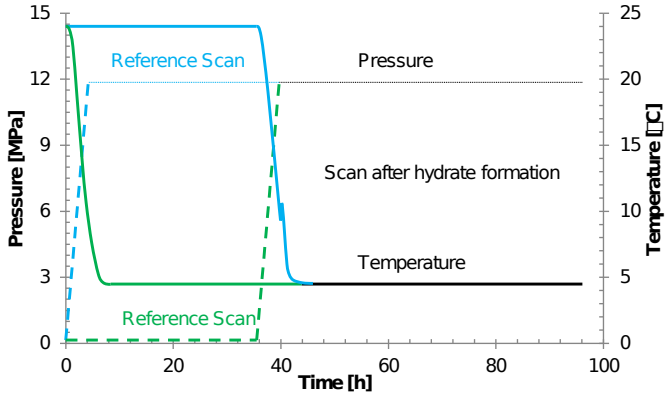
Flow through: Tests included: ExG-KI-3(KI), ExG-KI-2(KI), ExG-KI-1(KI).	
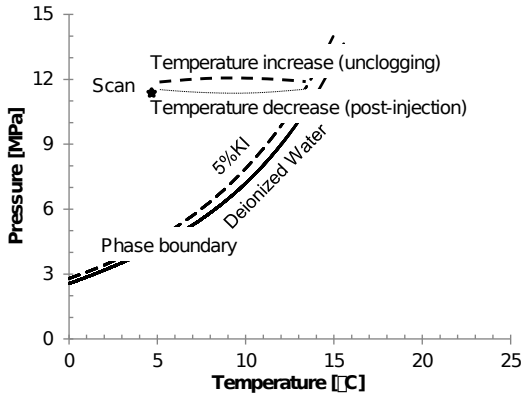	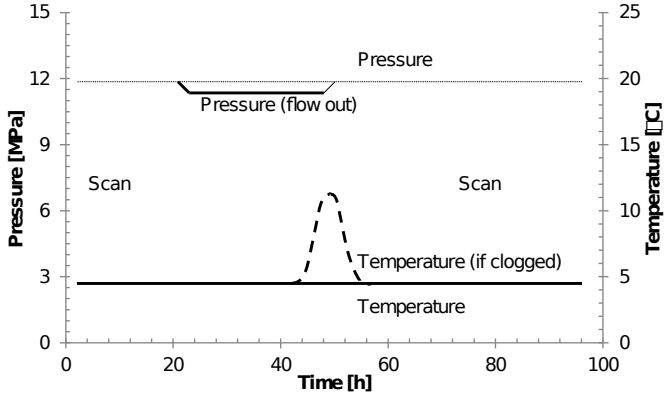
ExW: Tests included: ExW-1, ExW-2.	

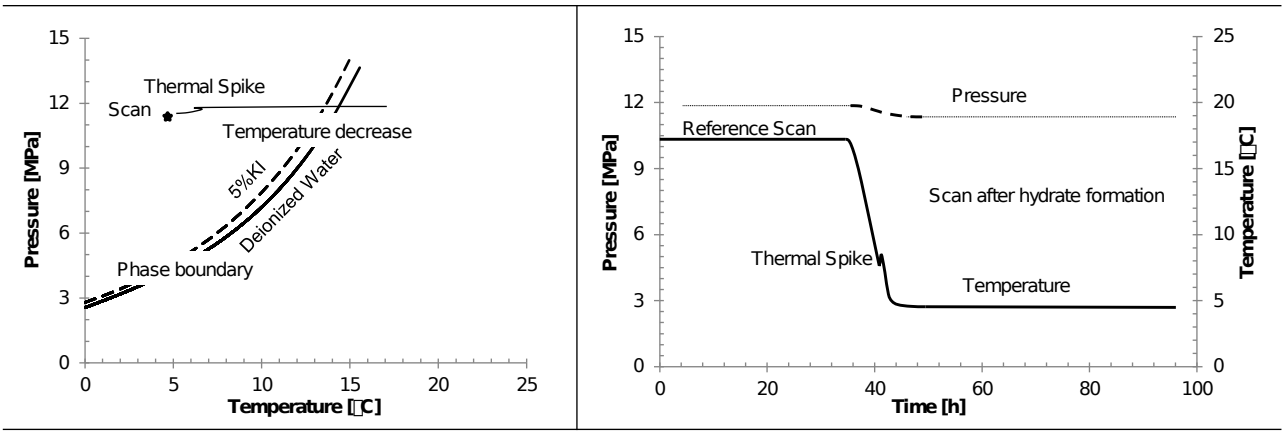

1027Figure 3. Pressure-temperature evolution during hydrate formation and dissociation.
1028a) Thermal spike indicating hydrate nucleation followed by pressure drop associated
1029gas consumption, and b) Freshening effect and the induced phase boundary shift
1030during hydrate dissociation.

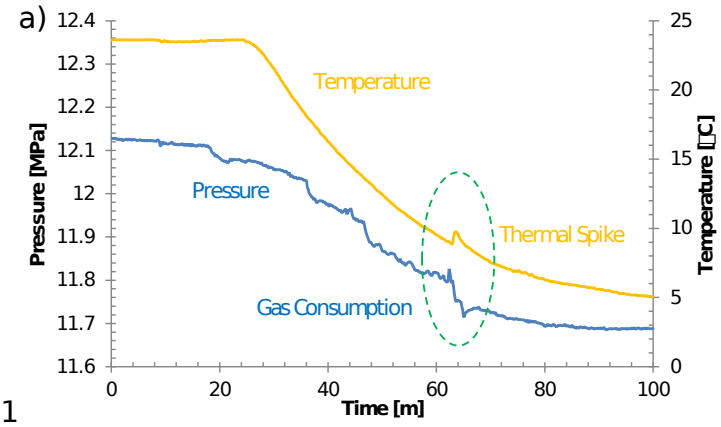

1031

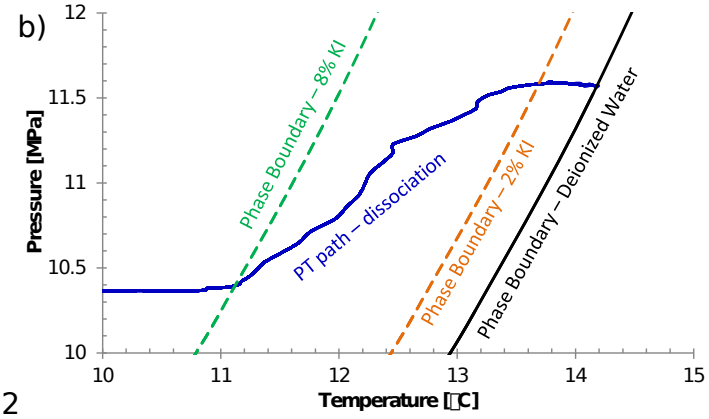

1032

Figure 4. Water migration during hydrate formation (ExG-2 in Table 1). a) Projection at 5 minutes after the thermal spike minus projection at the reference point before hydrate formation: blue area = mass loss, red area = mass gain; b) Projection at 81 hours after the thermal spike minus reference point; c) One vertical slice of the 3D reconstructed image: water is concentrated in the lower part; d) High resolution image that corresponds to the marked zone in c); e) Initial water distribution and hydrate evolution over 81 hours after thermal spike at two locations shown in d): Slice B gains water from surrounding to form hydrate but slice A loses all the water at the end.

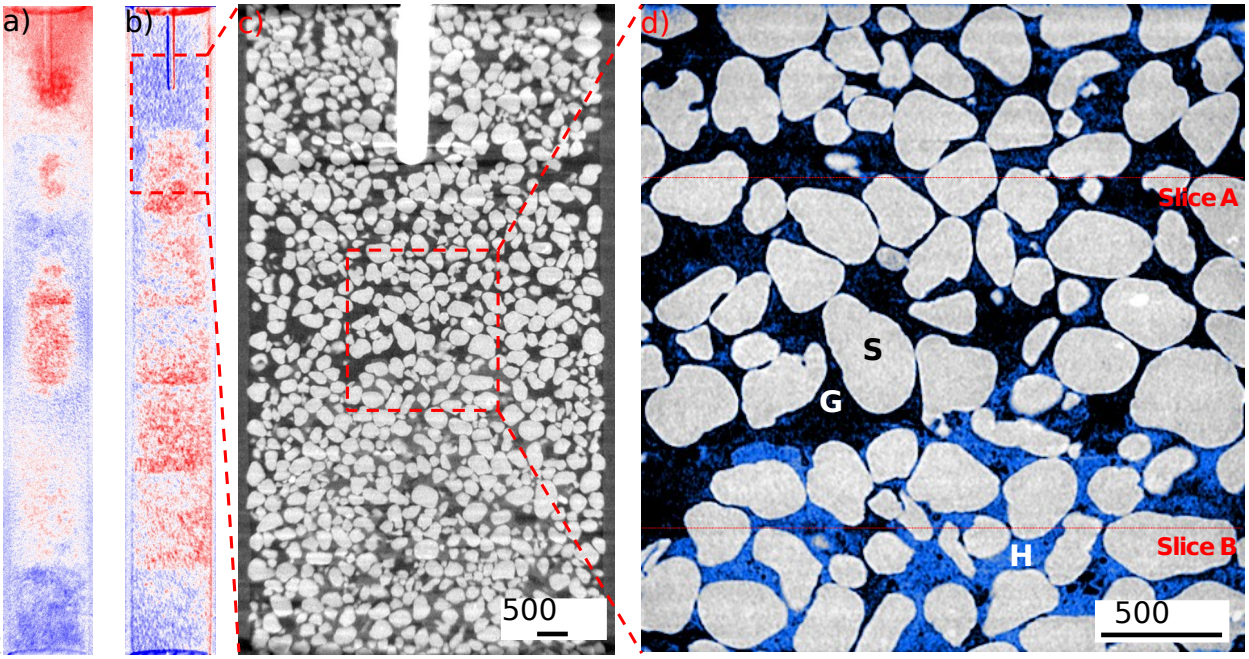

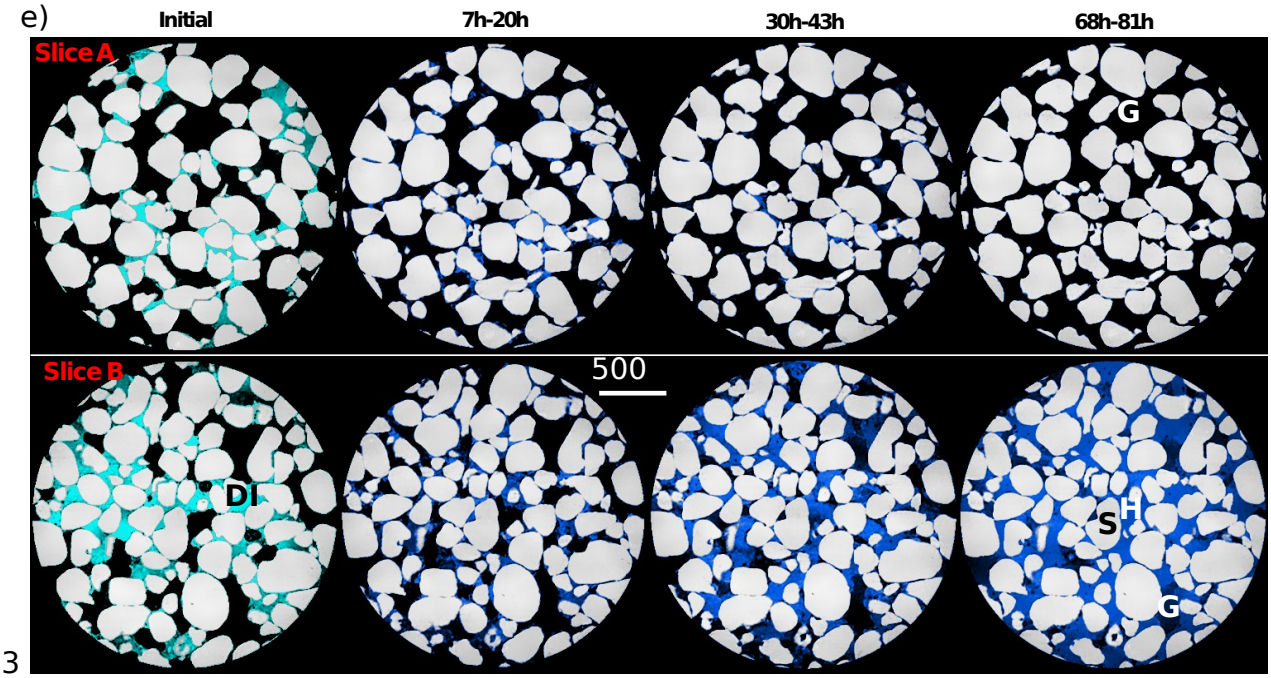

1044S=Sand Particle, DI=Deionized water in cyan, H= Methane Hydrate in blue, and 1045G=Methane Gas.

1046Figure 5. Hydrate saturation and pore habit resulting from hydrate formation under
1047gas-excess conditions. Most of the hydrate-gas boundaries are clear except in d),
1048where extended evolution is in progress. From a) to d) test number (time for
1049hydrate formation): ExG-1 (77h-149h), ExG-KI-1 (54h-74 h), ExG-KI-3 (80h-102h)
1050and ExG-2 (68h-81h).

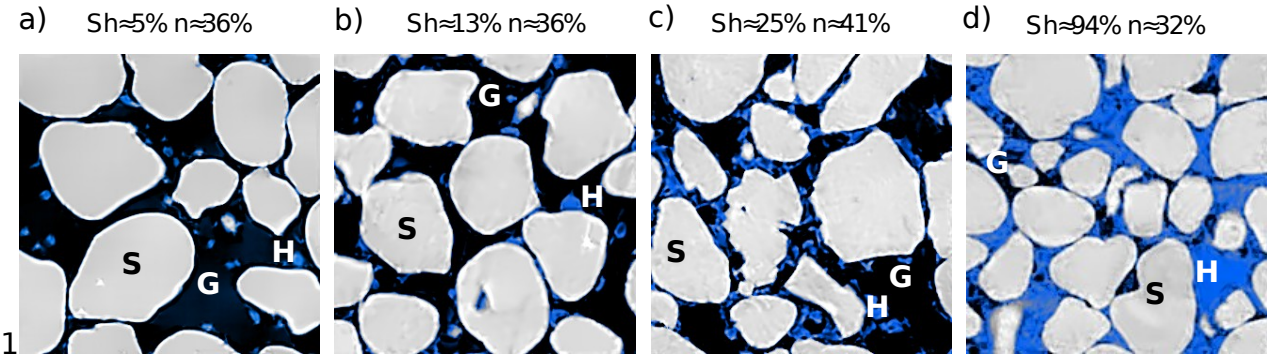

1051

1052S=Sand Particle, H=Methane Hydrate in blue, and G=Methane Gas.
1053

Figure 6. Hydrate morphology after KI solution injection. Injection occurs when the system is deep into hydrate stability field in a) (ExG-KI-3), c) and d), but close to phase boundary in b) (ExG-KI-2). c) and d) are from the same experiment (ExG-KI-1) but different locations in two layers of sand with Ottawa sand c) and F110 sand d). b) is scanned shortly after the injection, while the rest is in relative stable condition. Local hydrate saturation in d) is higher than in c) because the small pores in d) preserves more water initially before hydrate formation in excess gas condition.

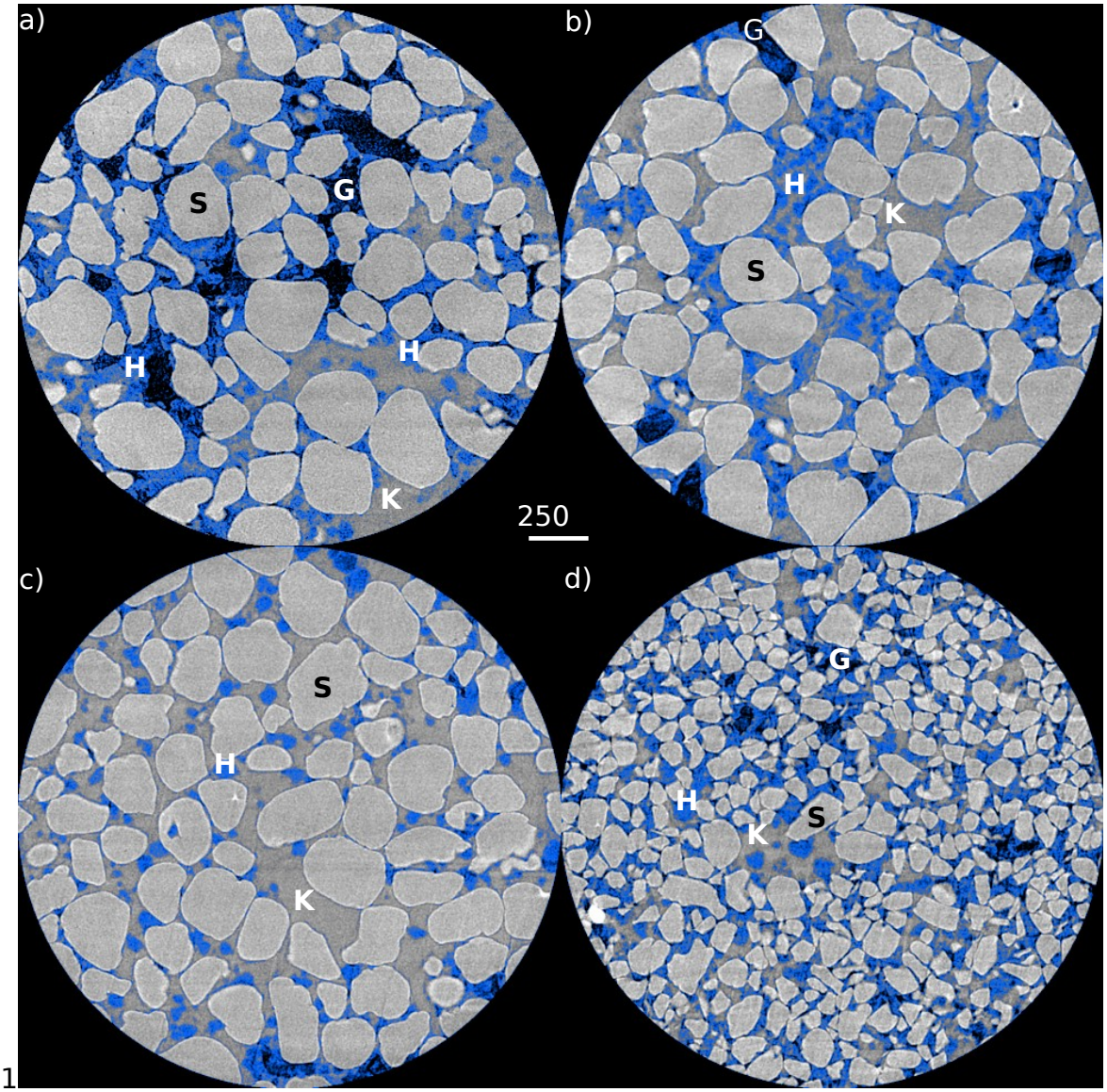

S=Sand Particle, KI=KI solution, H= Methane Hydrate in blue, and G=Methane Gas.

Figure 7. 3D view of hydrate formation in gas-excess system and its morphology evolution after brine injection deep inside hydrate stability field (ExG-KI-3). a) Initial state, b) 6-18 hours after thermal spike: hydrate formation in gas-excess system, c) 42-102 hours after thermal spike: hydrate evolution, d) 6-18 hours after KI solution injection, e) 24-36 hours after KI solution injection, f) 54-114 hours after KI solution injection, and g)-i) are 3D distribution of water and hydrate corresponding to the areas in the red boxes in a), c), and f) respectively. The majority of hydrate in h) evolves towards pore-filling in i) after brine injection; meanwhile yellow circled area in d) contains cementing hydrate formed in c) which remains until the end of experiment.

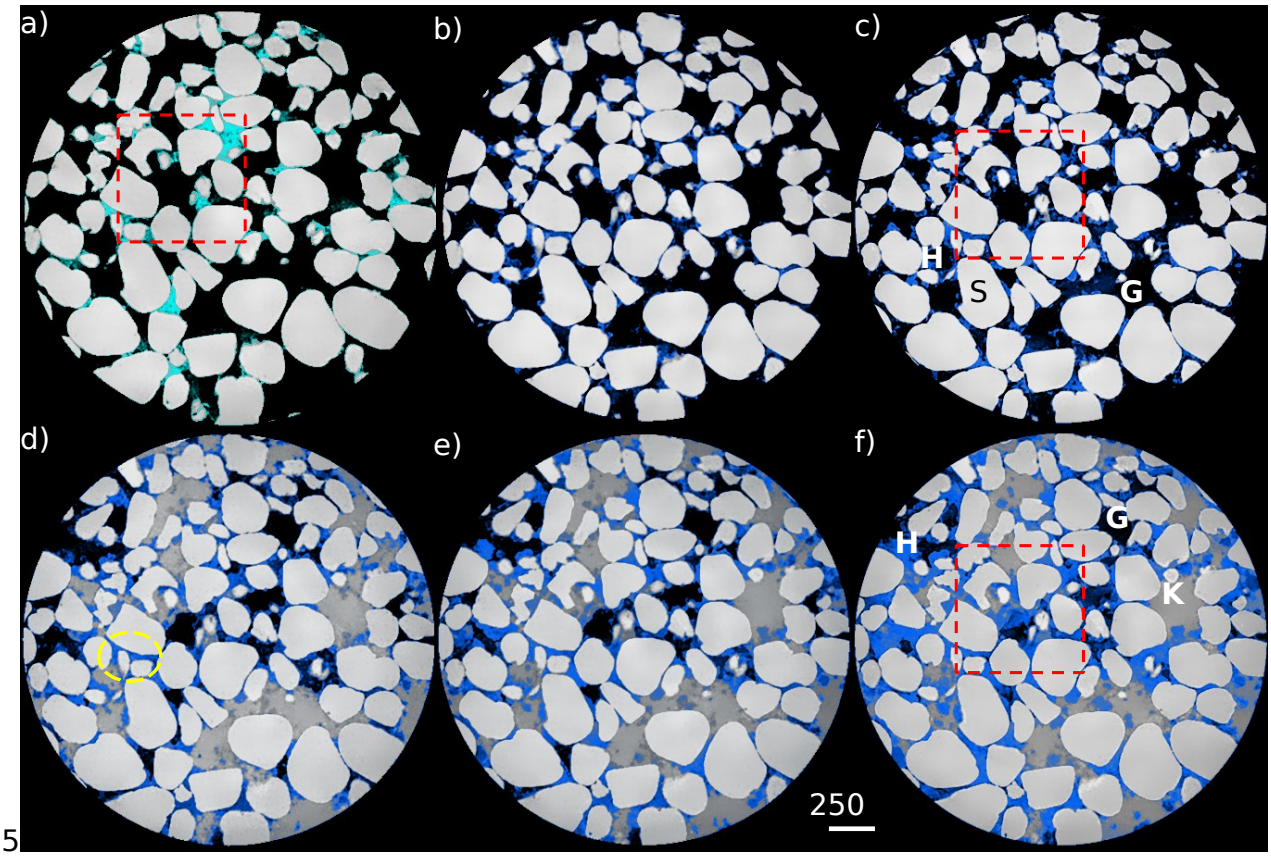

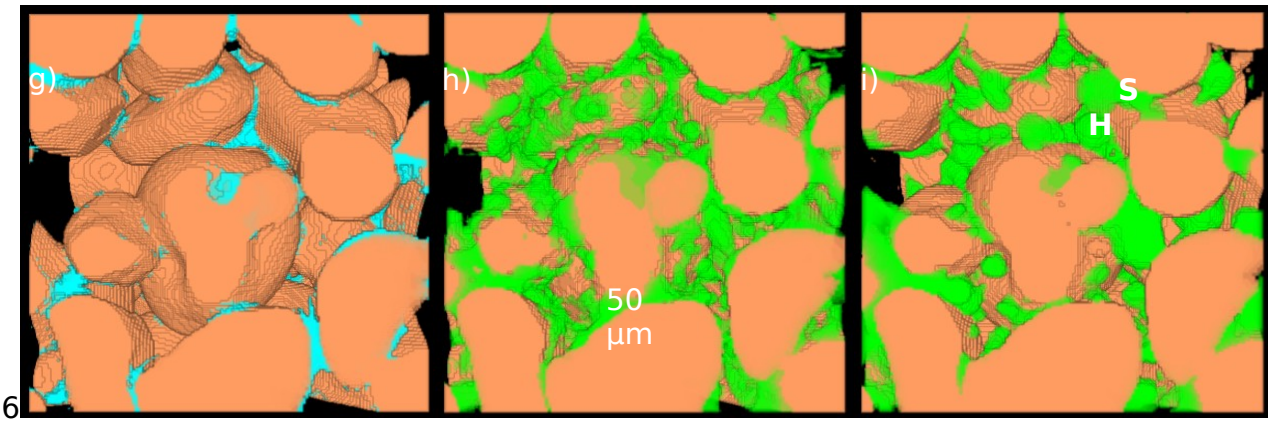

1077S=Sand Particle, KI=KI solution, DI=Deionized water in cyan, H= Methane Hydrate
1078in blue in b)-f) and in green in h) and i), and G=Methane Gas.

Figure 8. Hydrate formation in water-excess system (ExW-1). a) Initial state with smooth interfaces determined by Laplace equation between KI solution and methane gas, b) 6-18 hours after thermal spike: hydrate shell forms and some gas bubbles collapses, blue circles contain blurred gas pockets where brine invasion and hydrate shell breakage occur during the scan. The yellow circle contains hydrate spike that will be further explained in Figure 11. c) 30-42 hours after thermal spike: hydrate formation further invades into gas pockets (red and blue circles). The sand-gas interface in the red circle in a) is mostly covered by a layer of hydrate, showing grain coating hydrate growth, and d) 150-162 hours after thermal spike: most of the methane gas has been transformed into hydrate, earlier formed gas hydrate particles merge into larger but less hydrate particles (area in the green circle).

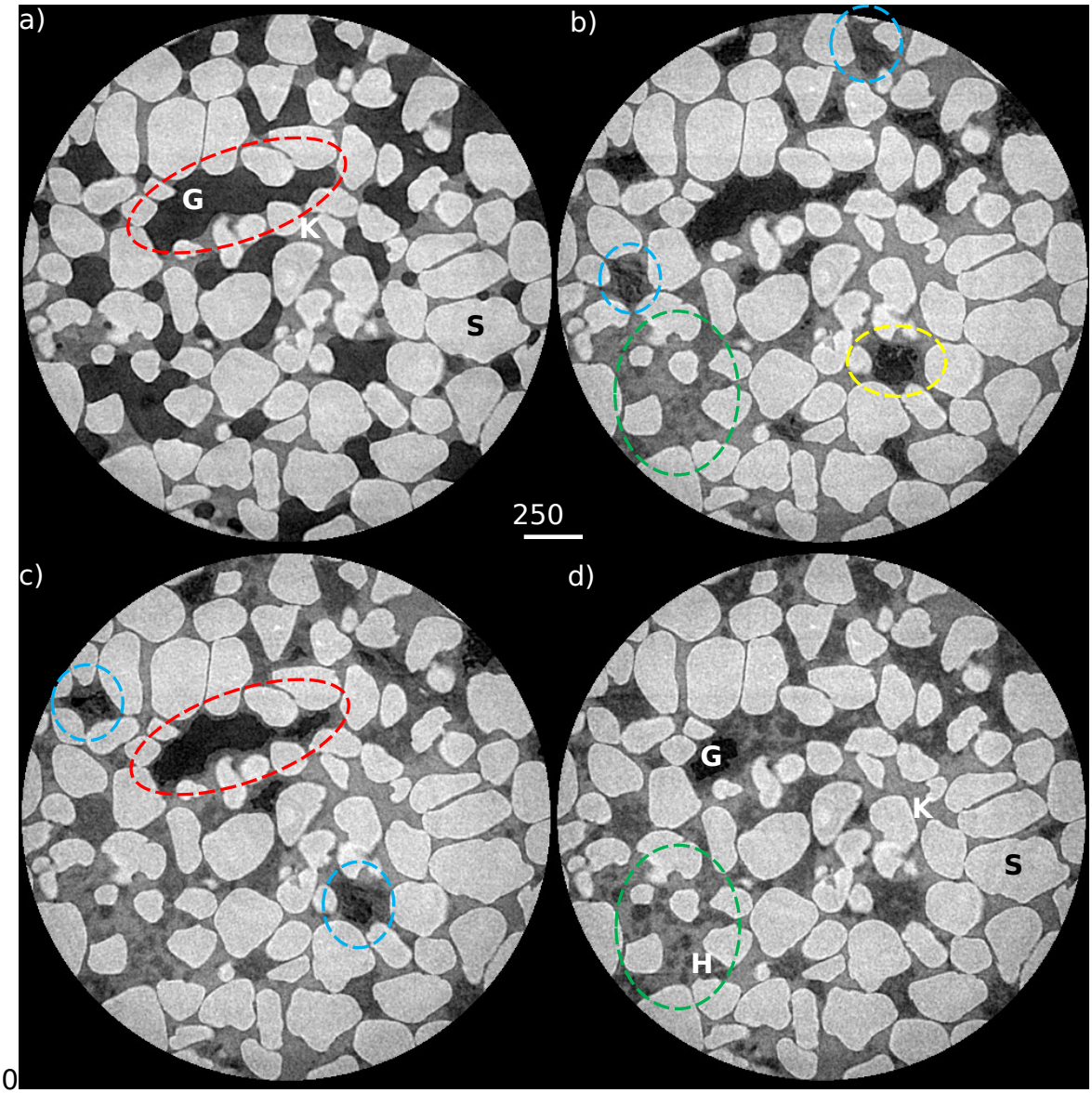

S=Sand Particle, KI=KI solution, H=Methane Hydrate, and G=Methane Gas.

Figure 9. Hydrate formation in water-excess system (ExW-2). Hydrate spikes form when deionized water is used initially as shown in yellow circled area. There is a layer of hydrate between gas and water, not by image intensity, but indicated by the complex morphology in the yellow circled area that differs from the smooth interface between water and gas without hydrate in Figure 8a), yet the thickness of hydrate shell cannot be determined in this image due to similar density and X-ray absorption capability between methane hydrate and deionized water.

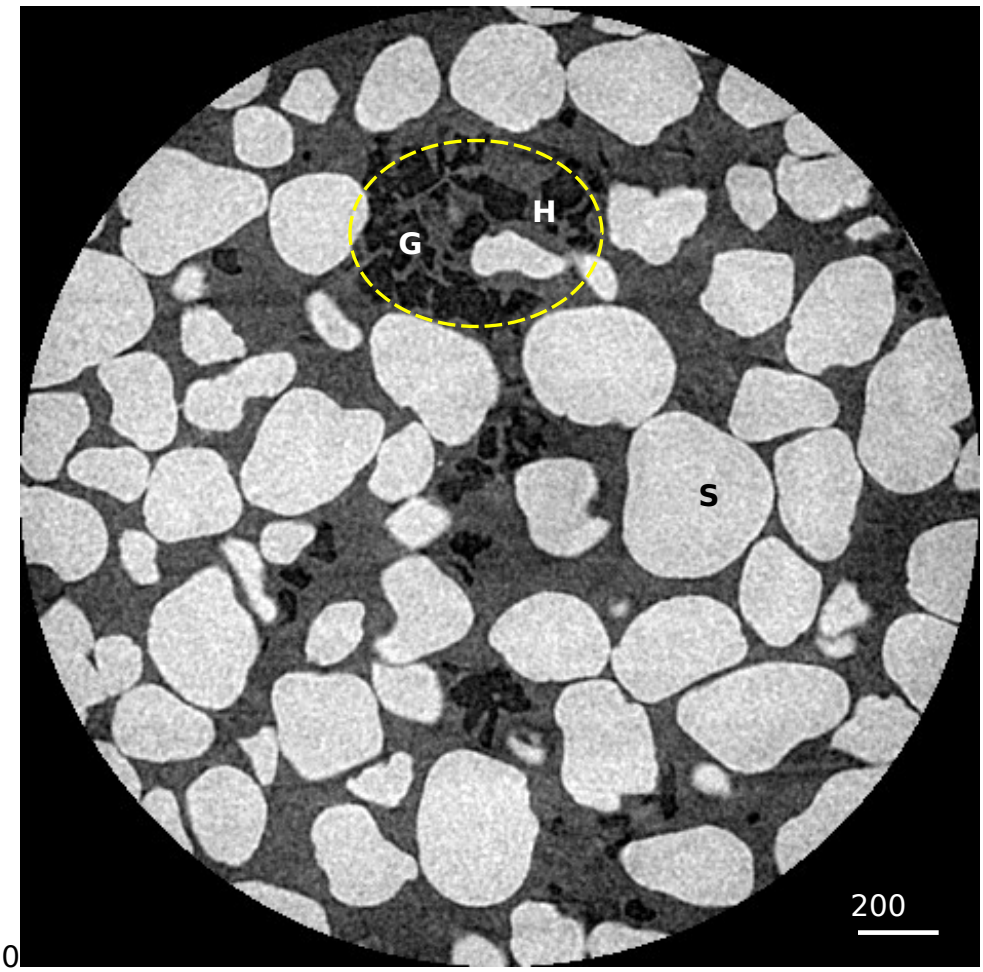

S=Sand Particle, H=Methane Hydrate, and G=Methane Gas.

1104Figure 10. Schematics showing mass migration during hydrate formation a)-c) and
1105contact angle d). a) Water migration via water film, b) Water migration via water
1106vapor through gas phase, c) Methane migration via diffusion of dissolved methane,
1107and d) Contact angle to show relative affinities to sand surface.

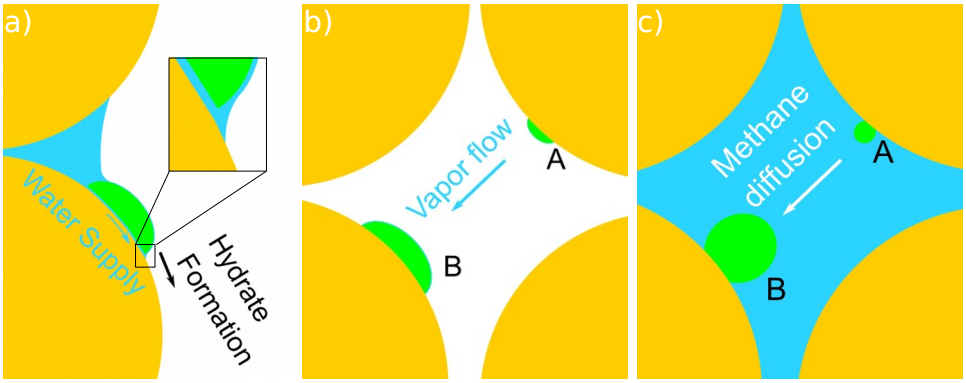

1108

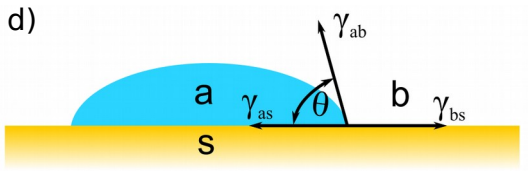

1109

1110

1111

Figure 11. Mechanism of hydrate spike formation (ExW-2 and ExW-1). a) and c) Hydrate spikes formation in deionized water environment, and b) and d) spikes in brine environment. The color intensity of brine in d) reflects the salt concentration. The length of spikes is shorter in brine condition due to ion-exclusion effect.